Title: Comprehensive Multi-omics Mapping of Vesicle Cargo from Plasma or Novel Tissue Vesicles Reveals Pathological Changes in Cargo with Patient Age

Authors: George Ronan[1], Lauren Hawthorne[1,2], Jun Yang[3], Ruyu Zhou[4], Fang Liu[4], Pinar Zorlutuna[1,2,3,5]*

[1]Department of Aerospace and Mechanical Engineering, University of Notre Dame, Notre Dame, IN, 46556, USA

[2]Bioengineering Graduate Program, University of Notre Dame, Notre Dame, IN, 46556, USA

[3]Department of Chemical and Biomolecular Engineering, University of Notre Dame, Notre Dame, IN, 46556, USA

[4]Department of Applied and Computational Mathematics and Statistics, University of Notre Dame, IN, 46556, USA

[5]Harper Cancer Research Institute, University of Notre Dame, Notre Dame, 46556, USA

*Corresponding author. Email: pzorlutu@nd.edu

Abstract: Aging is a major risk factor for cardiovascular disease, the leading cause of death worldwide, and numerous other diseases, but the mechanisms of these aging-related effects remain elusive. Recent evidence suggests that chronic changes in the microenvironment and local paracrine signaling are major drivers of these effects, but the precise effect of aging on these factors remains understudied. Here, for the first time, we directly compare extracellular vesicles obtained from young and aged patients to identify therapeutic or disease-associated agents, and directly compare vesicles isolated from heart tissue matrix (TEVs) or plasma (PEVs). While young TEVs and PEVs showed notable overlap of miRNA cargo, aged EVs differed substantially, indicating differential aging-related changes between TEVs and PEVs. TEVs overall were uniquely enriched in miRNAs which directly or indirectly demonstrate cardioprotective effects, with 45 potential therapeutic agents identified in our analysis. Both populations also showed increased predisposition to disease with aging, though through different mechanisms. Changes in PEV cargo were largely correlated with chronic systemic inflammation, while those in TEVs were more

related to cardiac homeostasis and local inflammation. From this, 17 protein targets were identified which were unique to TEVs and highly correlated with aging and the onset of cardiovascular disease. Further analysis via machine learning techniques implicated several new miRNA and protein targets, independently suggesting several of the targets identified by non-machine learning analysis, which correlated with aging-related changes in TEVs. With further study, this biomarker set may serve as a powerful, potential indicator of cardiac health and age which can be measured from PEVs. Additionally, several proposed “young-enriched” therapeutic agents were validated and, when tested, could successfully prevent cell death and cardiac fibrosis in disease-like conditions.

37 **Main Text:**

38 **INTRODUCTION**

39 Advanced age is quickly becoming the most prevalent risk factor worldwide for numerous
40 diseases, including cardiovascular disease (CVD), leading cause of death worldwide[1], obesity and
41 obesity-related diseases[2], and many cancers[3], and by 2050 the global population aged 65 or older
42 is expected to double to over 2 billion or nearly 20% of predicted global population[4]. In some
43 rapidly aging countries, such as Japan and Italy, 65+ aged individuals already account for over
44 20% of the population[5], with Japan quickly approaching 30%. Recent literature has implicated
45 long-term changes in the cardiac microenvironment in aging-related CVD pathogenesis[6–9], and
46 suggests that these changes can be manipulated to improve patient outcomes. The use of
47 extracellular matrix (ECM) or ECM-derived materials has seen some success in pre-clinical trials
48 by leveraging previously established effects of ECM treatment, including
49 immunomodulation[7,10,11], stem cell recruitment[7,12,13], and functional revitalization[6,12–14]. These
50 properties enhance the reparative effects of novel biomaterials, commonly being integrated with
51 hydrogels or other bioscaffolds in treatment of CVDs[9,10,13,15,16]. However, the mechanisms by
52 which ECM promotes these effects is not well understood, and the drivers of aging-related changes
53 in the microenvironment are critically understudied.

54 Extracellular vesicles (EVs) have been recently identified as potential agents of aging-related
55 changes in the microenvironment[6,7,14] and key mediators of many therapeutic effects observed in
56 ECM treatment[11,13,17]. However, many of these studies have been largely limited to EVs isolated
57 from plasma and have been identified as exosomes[18,19]. Exosomes are a specific subcategory of
58 small EV (sEV), or EVs with typical sizes of under 200 nm[20,21], that express characteristic surface
59 protein markers and serve as common vehicles for endocrine, paracrine, and even autocrine

60 transport of RNAs and proteins[21–23]. While more recent efforts have focused on the broader
61 category of sEVs, due to difficulties in separating exosomes from other sEV subgroups such as
62 supermeres and exomeres[7,24], exosomes have been investigated as "tissue-free" theragnostic
63 nanoparticles. Stem cell-derived exosomes are being investigated in a clinical trial as vital
64 components for an "off-the-shelf" cardiac patch that emulates the benefits of direct ECM
65 incorporation[13,25], and plasma exosomes have provided a wealth of real-time diagnostic
66 information for patients in both CVDs[15,26] and cancer diagnosis[27,28].

67 Tissue matrix-derived sEVs provide a unique avenue to evaluate the effects of aging-related
68 changes in the microenvironment on the progression of CVDs, a topic that has remained elusive
69 and difficult to address clinically[8,10,13,14,17,29]. While CVD-related mortality is often actuated by the
70 onset of myocardial infarction (MI)[1,30], the risk of mortality is predominantly regulated by a
71 combination of risk factors including previous cardiac event[30–32], obesity and metabolic health[30,33],
72 and age[34,35], and recent studies have clearly demonstrated correlative effects between age and the
73 risk of MI or chronic CVD[4,8,35–37].

74 Previously, we discovered and characterized cardiac tissue ECM-resident exosome-like sEVs from
75 donor hearts from young or aged donors, and found that the size, morphology, and miRNA and
76 protein contents of these sEVs significantly changed with donor age[7]. Despite a growing body of
77 literature supporting the use of sEVs as dynamic theragnostic tools in CVD and other diseases[9,17],
78 currently in literature there is no single resource that directly investigates and establishes aging-
79 related changes in sEV content for tissue-resident sEVs, and any head-to-head comparison of
80 miRNA and whole protein profiles of tissue-resident or plasma-derived sEVs is similarly absent.
81 This may be due to the relatively recent discovery of ECM-resident sEVs[38], but remains a notable
82 gap in knowledge.

83 Herein we, for the first time in literature, characterize differences in size profile, surface protein
84 distribution, and uptake mechanics of sEVs derived from cardiac tissue ECM, or tissue sEVs
85 (TEVs), and sEVs derived from plasma, or plasma sEVs (PEVs). We also establish previously
86 unreported differential aging-related changes in these metrics between TEVs and PEVs by
87 assessing both populations of EVs from young (<40 y.o., n = 6 for tissue & plasma) and aged (>50
88 y.o., n = 6 for tissue & plasma) donors. After this, we provide a whole miRNA profile for TEVs
89 and PEVs from young and aged donors, a dataset currently absent in literature, and identify targets
90 and pathways of interest for CVD within our dataset. Following this, we do the same for a whole
91 protein profile, again from TEVs and PEVs from both young and aged donors for the first time in
92 literature. From these analyses, we can successfully bifurcate the cargo profiles of TEVs and PEVs,
93 with PEVs tending to be largely correlated with systemic immune response and cardiac TEVs
94 tending to be related to cardiac homeostasis and CVD, as expected. TEVs were also uniquely
95 enriched in cardioprotective miRNAs involved in the regulation and prevention of fibrosis and
96 anoxia-related cell death. Most interestingly, aged-source EVs in both populations tended to
97 exhibit higher enrichment of cargo involved in disease-associated pathways than young-source
98 EVs not through nucleic acid cargo, but through chauffeured proteins. While the specific pathways
99 involved were different, with aged PEVs mostly trafficking proteins related to increases in chronic
100 systemic inflammation and neurological diseases and aged TEVs transporting proteins relating to
101 increased risk of heart failure, increased local inflammation, and overall metabolic shift, both
102 populations suggested that EVs can propagate aging-related damage-inducing proteins. From these
103 cargo analyses, we identified 45 miRNA targets which provide cardioprotective effects and 17
104 proteins which are implicated in the development of CVDs. Additionally, we utilize machine
105 learning algorithms to identify biomarkers of cardiac aging which can be detected from PEVs,

106 providing a quantitative, low-invasive method of assessing long-term cardiac health or heart "age".
107 In addition to the identification of biomarkers, this analysis also validated several identified
108 potential therapeutic miRNAs. These miRNAs, in combination with previously evaluated
109 therapeutic miRNAs, were applied to cells in an MI-like environment to improve recovery post-
110 MI, and successfully improved survival of both muscle and stromal cells.

111 With these data we achieve several goals. First, we provide a resource for future studies
112 investigating aging-related changes in tissue-resident sEVs, a recently discovered source of EVs
113 that are currently poorly understood but provide exciting avenues for understanding and
114 manipulating disease-related intra-tissue signaling. Second, we contrast both these tissue-resident
115 EVs and classical plasma EVs as well as directly assess aged and young cargo from both
116 populations to identify aging-related changes in EV content and signaling, a sorely understudied
117 topic in EV research. Third, from the EV cargo we have identified both therapeutic miRNAs and
118 damage-associated protein cargo to direct future target-based studies and drug development for
119 notoriously difficult to target diseases, such as cardiac fibrosis. The dissemination of these data
120 will help promote more in-depth study of sEVs as both diagnostic and therapeutic vehicles to
121 investigate the effects of chronic changes to tissues, such as aging, and provide a useful tool for
122 the future investigation of comprehensive comparison of sEV populations. Fourth, we identified
123 both miRNA and protein biomarkers which, in TEVs, were indicative of aging and related to CVD
124 onset, but could also be identified from PEVs of aged donors. These biomarkers suggest that, with
125 greater understanding of aging-related changes in PEV and TEV cargo, it will be possible to
126 identify quantitative biomarkers of tissue aging from PEVs, as opposed to biopsy or similarly
127 invasive techniques. Lastly, we validated our previous hypothesis that further comparison of TEVs
128 and PEVs from differentially aged cohorts would identify further therapeutic miRNAs[7]. While this

129 therapeutic demands further testing, the therapeutic efficacy of this cocktail in a simple lipid
130 nanoparticle delivery mechanism compared to TEVs directly is an indicator that the therapeutic
131 effects of TEVs can in fact be reconstructed from specific, young-enriched cargos.

132 **RESULTS**

133 ***Characteristics of sEV size profile change depending on biological source:*** Transmission
134 electron microscopy (TEM) of sEVs isolated from tissue (TEVs) or plasma (PEVs) of young (<40
135 y.o., n = 6 for tissue & plasma, Supplemental Table S1) and aged (>50 y.o., n = 6 for tissue &
136 plasma, Supplemental Table S1) donors showed that all particles were similar in overall
137 morphology and staining characteristics (Figure 1A). sEV size profile was validated via
138 Nanoparticle Tracking Analysis (NTA), and the resultant statistics showed that size was mostly
139 consistent between young and aged samples in PEVs (young mode: 129.5 nm; aged mode: 159.5
140 nm) but not TEVs (young mode: 128.5 nm; aged mode: 49.5 nm) (Figure 1B). Furthermore, TEVs
141 were predominantly smaller than PEVs overall, although all sEVs fell within the expected size
142 range for exosome-like sEVs. All populations were found to be monodisperse, though young
143 tissue-source TEVs had a notably larger PDI than any other cohort (Supplemental Table S2).

144 ***Different tissue source sEVs demonstrate differential responses to aging effects:*** Western blot
145 was performed to identify characteristic exosome markers CD9, CD63, and TSG101 on the sEVs
146 isolated, with each protein showing up clearly (Figure 1C). The measured quantity of each protein
147 was also assessed from the blot using ImageJ for standardized blot quantification, and the results
148 were Z-scored for comparison (Figure 1D). These show that changes in expression of these
149 particular exosomal surface proteins behave inversely with respect to age between TEVs and
150 PEVs, with PEVs showing a 0.5-fold to 1-fold decrease in expression of CD9 and CD63 between
151 the young and aged cohorts and TEVs showing a greater than 1-fold increase in expression across

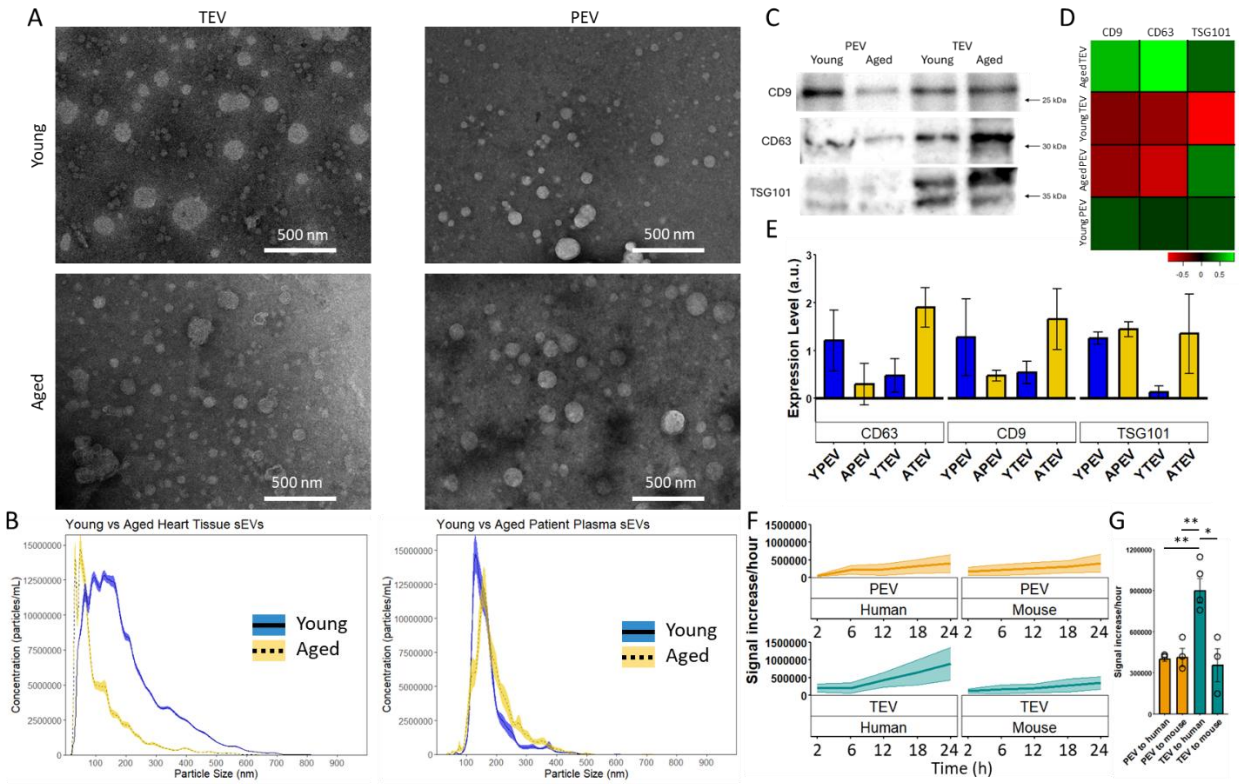

Figure 1. Tissue resident sEVs display substantive differences from those isolated from plasma in size profile, surface protein expression, and behavior. Measurements were taken from n = 6 biological replicates per cohort, equally spread between male and female donors. (A) Transmission electron microscopy representative images for each cohort. (B) Nanoparticle tracking analysis differentiating young (blue) or aged (gold) source tissue sEVs (left) or plasma sEVs (right). The overall expression of exosomal surface proteins was measured by western blot (C) and compared (D) and the change in expression between groups was compared with respect to tetraspanin (E). (F) Uptake rate of TEVs or PEVs from young donors (n >= 3 for each) on human or mouse fibroblasts in 2D culture (n >= 3 replicates for each) over 24 hours, presented as change in uptake rate per hour between timepoints taken ± standard error. (G) Endpoint uptake rate of TEVs or PEVs on human or mouse fibroblasts, bars represent mean of biological replicates ± standard deviation and points represent mean of replicates for each biological replicate. * $p < 0.05$, ** $p < 0.01$, assessed by Welch's t-test for (E) and (G).

167 that same comparison (Figure 1E). CD63 expression remained mostly consistent with CD9
168 expression in both populations with respect to age, though the change in expression was opposite
169 between TEVs and PEVs, but TSG101 availability was increased with age only in TEVs while
170 remaining consistent in PEVs, although it should be noted that these differences were not
171 significant with the metrics used. Taken with the above results, this suggests a shift in the
172 tetraspanin web and targeting abilities[39–41] that substantially differs between the TEVs and PEVs
173 for the proteins assessed.

174 ***Uptake kinetics of sEVs varies between tissue source and destination tissue:*** Uptake kinetics of
175 sEVs with typical or atypical cell culture populations was also assessed (Figure 1F). When applied
176 to murine cells, both PEVs and TEVs maintained steady uptake by cells over 24 h, resulting in a
177 nearly flat line (right). When applied to human cardiac cells, however, PEVs showed a slight
178 increase in uptake over time whereas TEVs showed exponential increase in uptake rate over 24 h,
179 reaching several-fold higher uptake rates and uptake overall than PEVs (Figure 1G). Additional
180 assays with young vs aged cells (artificially aged iCFs or aged mice) showed that the age of the
181 cell had no significant effect on either the uptake rate of EVs or the size of the EVs produced
182 (Supplemental Figure S1), an unexpected result.

183 ***Profiling of miRNA content:*** miRNA profiling via Nanostring analysis revealed highly distinct
184 miRNA profiles between PEVs and TEVs (Figure 2A), with sources tending to cluster together
185 both when compiled and in individual replicates (Supplemental Figure S2). While sEVs from
186 young donors of both sources showed some notable overlap, the miRNA profiles of sEVs from
187 aged donors were almost completely distinct, with less than 100 miRNAs in common. Relative
188 expression values for all 798 detected miRNA expressed in these samples is provided in the
189 supplement (Supplemental Table S3). Prevalence of miRNAs in all sEVs was mostly normally

190 distributed (Figure 2B), though both PEV populations had a notable number of very highly
191 expressed (detected count >30 in chip) miRNAs. In general, sEVs from young donors tended to
192 express a larger number of miRNAs overall but at lower counts, while sEVs from aged donors
193 tended to express fewer miRNAs but at higher concentrations, consistent with previous findings[7].
194 Unsupervised analysis of the data to identify distinguishing miRNAs between TEVs and PEVs
195 revealed 125 potential targets (Figure 2C). Of these 125 miRNAs, 59 were expressed in TEVs but
196 not PEVs, and 66 were highly expressed in PEVs but not TEVs (Supplemental Table S4).

197 ***Profiling of protein content:*** Protein profiling via mass spectrometry and subsequent analysis
198 revealed that TEVs and PEVs tended to separate into two distinct clusters depending on tissue
199 source, although this was less consistent when comparing individual biological replicates
200 (Supplemental Figure S7). This may be due to some proteins being entirely absent from detection
201 in many biological replicates (Figure 2D). Visualization of the overall protein population in terms
202 of prevalence or absence of proteins by number also revealed that many proteins were enriched
203 inconsistently between biological replicates, with less than 500 (< 20% of all identified proteins
204 via mass spec) were universally present in any given cohort, and a similar number was universally
205 absent in every cohort. To present a more readily comparable visual, the 93 proteins common
206 across all biological replicates for all cohorts were also mapped (Figure 2E, Supplemental Figure
207 S7, Supplemental Table S7). While in the overall population TEVs showed a slightly higher
208 overall protein enrichment, with aged donor TEVs still having higher overall protein enrichment
209 than young donor TEVs, comparison of only the common proteins across all replicates revealed a
210 substantial increase in enrichment in aged donor TEVs compared to all groups while young donor
211 TEVs displayed notably low levels of relative protein enrichment. Further subdivision of cohorts
212 by sex in addition to age additionally reveals that this is not a sex-dependent shift, though the

213 overall protein enrichment may be sex-dependent (Supplemental Figure S8). This is consistent
214 with our previous findings on relative protein content between aged and young donor TEVs[7].

215 ***Aging-correlated shifts in protein profile is similar between TEVs and PEVs:*** Breakdown of
216 protein enrichment by cohort was recorded via Venn Diagram (Figure 2F), and reveals that overall
217 both TEVs and PEVs have a similar number of overlapping and distinctive protein cargo. Both
218 populations, however, show similar changes in cargo with respect to age. In both TEVs and PEVs,
219 comparison of young donor sEV unique protein contents with that of aged donor sEV content
220 reveals a nearly 3-fold increase in unique proteins consistently expressed in all biological
221 replicates. Aged donor TEVs have a higher number of unique proteins compared to TEVs.

222 ***Mapping of miRNA targets implicates TEV signaling in multi-point regulation of***
223 ***cardiovascular health-related pathways:*** Of the 59 miRNA targets overexpressed in TEVs, 45
224 have been identified as "potentially involved" in CVD according to PubMed and other online
225 databases[26]. These 45 miRNAs were pulled out and visualized (Figure 3A), evaluated for potential
226 gene targets and overlap (Figure 3B, C), assessed via gene ontology (Figure 3D), and mapped
227 using MetaCore Pathway Analysis (Figure 3E-H). Likely gene targets were assessed for
228 overlapping targets of miRNAs and contributions of miRNAs to individual gene targets. Analysis
229 revealed 11,366 potential gene targets (Supplemental Table S5), though more than two-thirds were
230 targeted by only a single target miRNA. Of the target miRNAs, miR-519, miR-181, and miR-548
231 contributed to the largest number of gene targets (Supplemental Figure S4). Genes which were
232 targeted by 10 or more target miRNAs were selected for gene ontology analysis, resulting in
233 selection of 167 genes (Supplemental Figure S4, Supplemental Table S6). Within this cohort of
234 genes, miR-548 and miR-519 remained the top contributors with miR-129 supplanting miR-181,
235 though miR-181 remained a major contributor (Figure 3B). The top 10 targeted genes were also

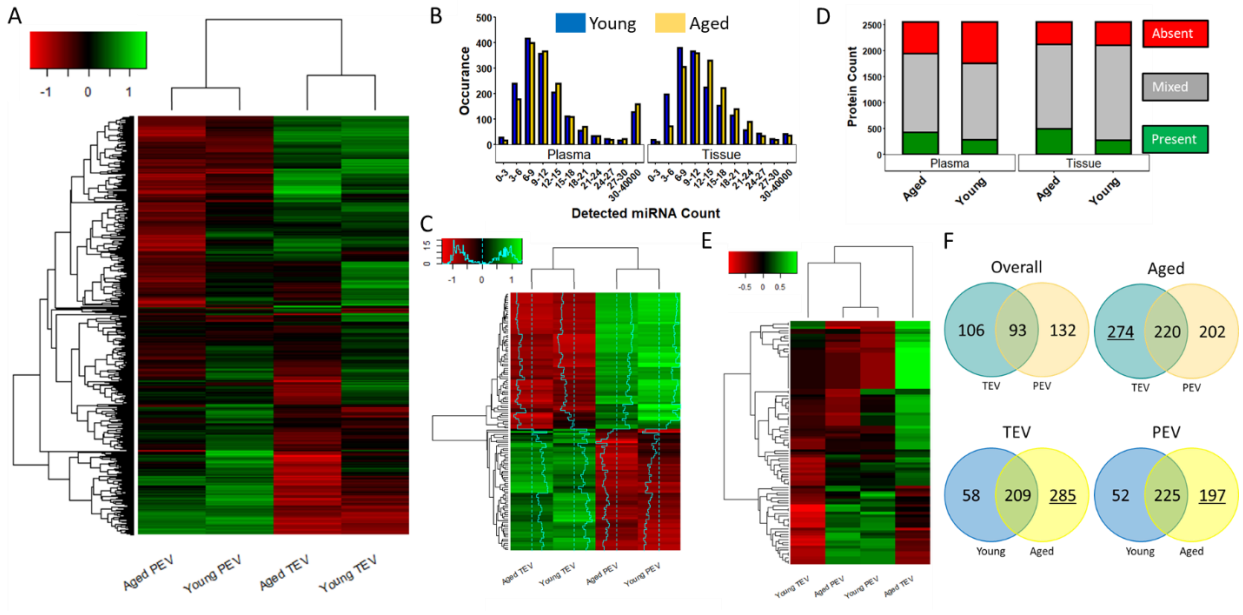

Figure 2. Summary of total miRNA and protein profile from tissue or plasma-source sEVs. Measurements were taken from n = 6 biological replicates per cohort, equally spread between male and female donors. (A) Heatmap showing the full miRNA profile for each cohort. Supplementary figures are available for individual replicates (Supplemental Figure S2) and for separation by both age and sex (Supplemental Figure S3) of total miRNA profile. (B) Histogram detailing the overall prevalence and distribution of miRNAs measured for each cohort. (C) Heatmap of the miRNA targets identified via unsupervised analysis that distinguish between TEVs and PEVs. A total of 125 miRNAs were identified and were nearly evenly split between TEVs and PEVs, with TEVs overexpressing 59 miRNAs and PEVs claiming 66. A full list of these miRNAs can be found in the supplement (Supplemental Table S4). (D) Stacked bar plot showing the expression profile of all 2547 detected proteins for individual cohorts, separating between proteins that are absent in all biological replicates (red, top), present in all biological replicates (green, bottom), or neither (grey, middle). (E) Heatmap showing the relative expression of the 93 proteins that were expressed in every biological replicate across all cohorts (Supplemental Table S7). Supplementary figures are available of all 2547 detected proteins for cohorts and individual replicates (Supplemental Figure S7) and for separation by both age and sex (Supplemental Figure S8) of both protein profiles. (F) Venn diagrams showing overlap of "present" proteins across cohorts, comparing between TEVs and PEVs overall (top left), only aged donor TEVs and PEVs (top right), young and aged donor TEVs (bottom left), and young and aged PEVs (bottom right). In comparisons where one side shows >33% greater quantity of proteins, the number of proteins was underlined.) * $p < 0.05$.

258 identified (Supplemental Figure S5) along with contributing miRNAs (Figure 3C, Supplemental
259 Figure S5). Of the top 10, the disruption of regular signaling for ZBTB20, CLOCK, TNRC6B,
260 RORA, CREB1, MECP2, MINDY2, TAOK1, and AAK1 was linked to cardiovascular disease[42–
261 51], typically through analogous pathways to chronic CVD or similar chronic fibrosis diseases
262 although many of these genes were also identified targets in neurological disorders and ischemic
263 stroke. Gene ontology analysis of the 167 common gene targets was largely unsurprising, though
264 there was noted involvement in cellular metabolism, macromolecule biosynthesis, and cAMP, co-
265 SMAD, and JNK-kinase activity (Supplemental Figure S6). MetaCore analysis of the 45 miRNA
266 targets revealed four major pathways of interest which were regulated at several points by different
267 identified miRNAs along the pathway (Figure 3E-H), suggesting deliberate targeting of certain
268 pathways in a highly specific manner. The pathways of interest were the HNF4-a pathway (Figure
269 3E), with downstream regulation that promoted exosome trafficking and inhibited inflammation
270 and apoptotic signaling[52–56], the Smad3/STAT5 pathway (Figure 3F), with overall inhibition of
271 signaling early in the Ang2 cardiac fibrosis cascade[57–62], PPARg pathway/MAPK cascade (Figure
272 3G), with more multi-point regulation of Ang2-mediated fibrosis signaling and downstream targets
273 parallel to the HNF4-a pathway[63–67], and an SDF-1a/systemic stem cell recruitment pathway
274 implicated in pro-regenerative healing from MI[68–73] (Figure 4H).

275 ***Gene ontology reveals functional differences in protein content between TEVs and PEVs:*** The
276 proteins enriched in TEVs or PEVs were also assessed via gene ontology analysis (Figure 4A, B).
277 Both TEV and PEV proteins were closely associated with extracellular vesicles and the
278 extracellular space, as expected, however the associated biological processes predicted were
279 notably different. TEVs were identified with muscular development and function (Figure 4A) as
280 well as a number of pathways corresponding to specifically cardiac development and homeostasis

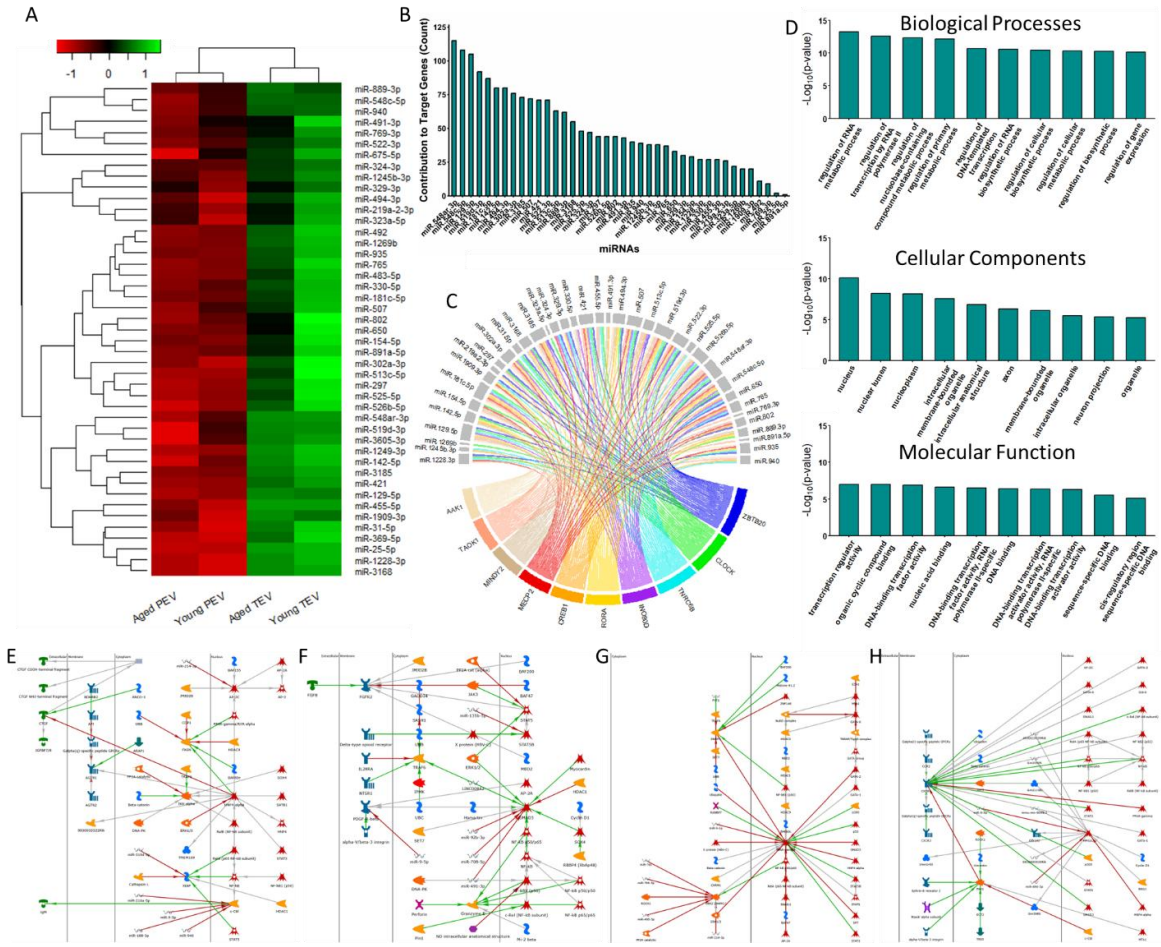

Figure 3. Cardiovascular-disease related target miRNAs and identified pathways identified from age and sex-related differences in sEV miRNA profile. Measurements were taken from n = 6 biological replicates per cohort, equally spread between male and female donors. (A) Heatmap showing identified target miRNAs enriched in TEVs relative to PEVs. (B) Analysis of miRNA contributors to predicted gene targets, showing by number the frequency of miRNAs contributing to different identified target genes (full gene list available in Supplemental Table S5). (C) Chord diagram showing overlap of miRNAs and the top 10 enriched predicted gene targets. (D) Gene ontology analysis of the predicted gene targets of the identified miRNAs showing the top 10 significant pathways identified (full graphs available in Supplemental Figure S6). (E-H) Results of MetaCore pathway analysis for the identified target miRNA data. * $p < 0.05$. Identified pathways were considered for analysis only for p-value < 0.05.

293 and redox pathways (Supplemental Figure S9). PEV proteins, alternatively, corresponded more to
294 acute inflammatory response and related pathways (Figure 4B), and was associated with IgG and
295 other immunoglobulins and components (Supplemental Figure S9). Interestingly, the gene
296 ontology analysis returned no significant results for molecular functions pertaining to PEV
297 proteins.

298 ***Tissue-resident sEVs showcase greater involvement in metabolism and homeostasis than***
299 ***plasma sEVs:*** Proteomap profiles (Figure 4C) were generated from the unique proteins identified
300 for both TEVs (106 proteins) and PEVs (132 proteins) (Supplemental Table S8), as well as for
301 aged donor TEVs (274 proteins) and PEVs (202 proteins) (Supplemental Table S9). Interestingly,
302 overall TEV pathways were balanced between metabolism, cardiac muscle activity, and
303 environmental signal transduction, whereas overall PEV pathways were dominated by
304 immunoregulation and exosome handling. Overall TEVs also uniquely called a pathway for
305 degenerative diseases (black, far left, top left proteomap). Aged donor sEV protein pathways,
306 however, were fairly different. Aged donor TEVs showed less overall involvement in cardiac
307 muscle activity and greater involvement in environmental signaling and metabolism. Aged donor
308 TEVs, compared to overall, also became newly involved in immunoregulatory signaling as well
309 as developing pathways associated specifically with cancer development, hypertrophic
310 cardiomyopathy, and arrythmogenic right ventricular cardiomyopathy, as opposed to the
311 previously observed degenerative diseases. Aged donor PEVs on the other hand became solely
312 dominated by immunoregulatory signaling, excluding exosome handling almost entirely, and
313 developing involvement in pathways associated with Alzheimer's Disease. Potential individual
314 protein targets were also identified from the unique proteins from TEVs and PEVs via supervised
315 analysis (Figure 4D). These 17 proteins, while not necessarily directly implicated in major

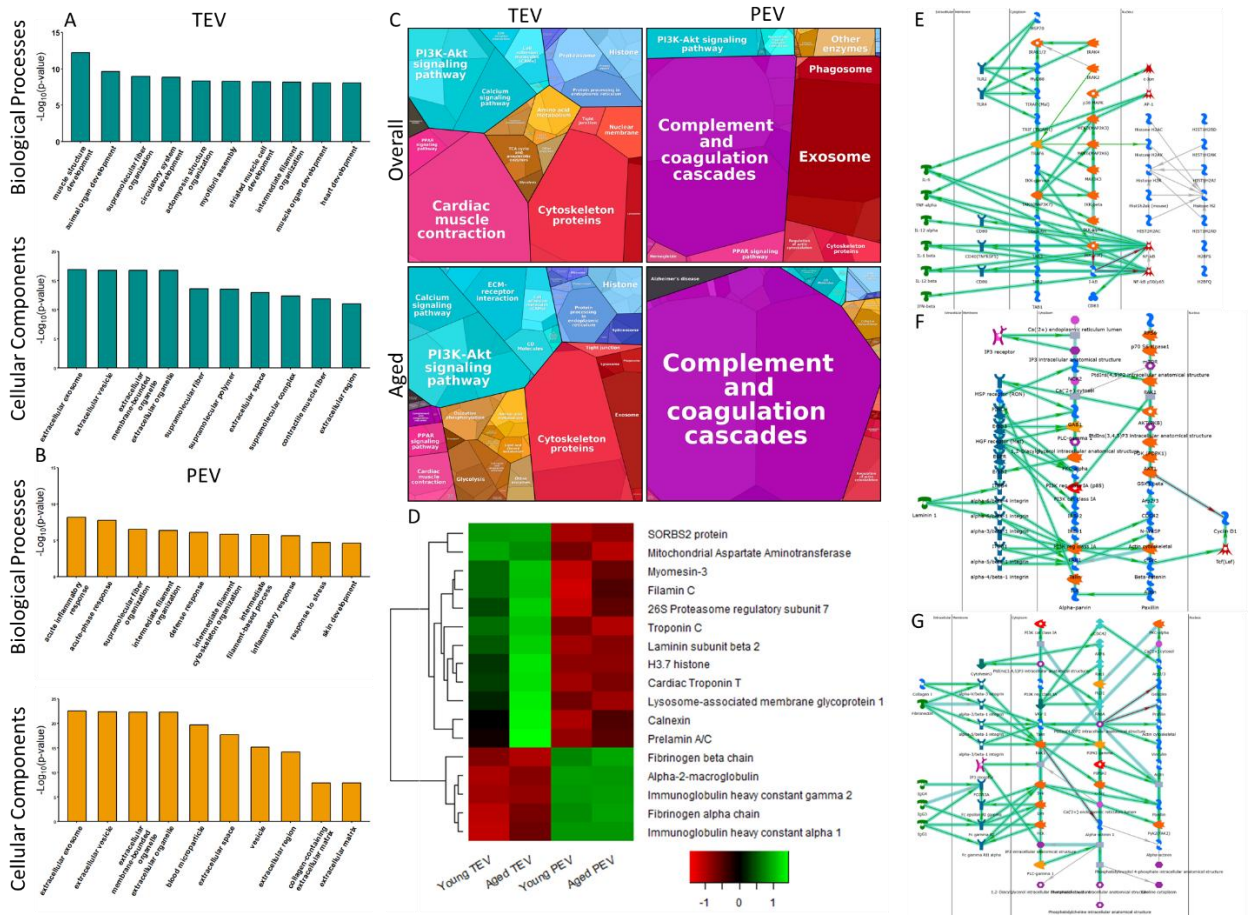

Figure 4. Cardiovascular-disease related target proteins and identified pathways identified from age-related differences in sEV protein contents. Measurements were taken from n = 6 biological replicates per cohort, equally spread between male and female donors. Gene Ontology Analysis results for TEVs (A) and PEVs (B) enriched in each population. Full graphs can be viewed at Supplemental Figure S9. (C) Proteomaps showing the KEGG pathways affected by the unique protein profiles of TEVs and PEVs overall, as well as for only aged donor TEVs and PEVs. Red: cellular processes; Yellow: metabolism; Pink: organismal systems; Blue: genetic information processing; Teal: environmental information processing; Purple: immune system; Black: human diseases. (D) Heatmap showing the 17 proteins of interest identified by supervised analysis of unique proteins for TEVs and PEVs. (E-G) Results of MetaCore pathway analysis for the unique protein profiles of TEVs (E, F) or PEVs (G). * $p < 0.05$. Identified pathways were considered for analysis only for p-value < 0.05.

330 pathways, are common biomarkers for identification of disease state or other pathology and may
331 allow for more rapid detection of critical marker quantification in clinical scenarios.

332 ***Tissue-resident sEVs from older hearts are directly implicated in CVDs, but not plasma sEVs***
333 ***from older patients:*** The unique proteins from TEVs and PEVs were mapped via MetaCore
334 pathway analysis, and the resulting pathways provided further insight into the downstream
335 activities of TEVs (Figure 4E, F) and PEVs (Figure 4G). TEV proteins mediated NFkB/Interleukin
336 signaling downstream of c-Jun and TRAF6 (Figure 4E), activities highly involved in cardiac
337 immunoregulation and matrix homeostasis[74–78], as well as directly interfacing with PI3k-1a,
338 mTOR, and Laminin response (Figure 4F), which together can be implicated in response to cardiac
339 fibrosis or other cardiac matrix remodeling[79–85]. Additionally, dysregulation of PI3k-1a and mTOR
340 via the complex "PI3K/mTOR signaling pathway" network has been directly implicated in aging-
341 related CVD onset and other aging-related pathologies, and the targeted inhibition of this pathway
342 has reversed aging-related risk of post-MI cardiac fibrosis and pathological signaling post-cardiac
343 insult[86,87]. PEVs also interacted with the surrounding matrix through integrin mediation (Figure
344 4G) but displayed more focus on modulating interactions with white blood cells via Igg
345 manipulation, which may indicate a role in chronic inflammation in chronic CVD and heart
346 failure[88–90].

347 ***Machine Learning Approaches Identify Novel Markers of Cardiac Aging***: Variable selection
348 techniques were applied to identify biomarkers that differentiate between young and aged cohorts
349 for TEVs and PEVs and between TEV and PEV cohorts young and aged EVs (Figure 5A). This
350 analysis revealed 42 potential miRNA targets for distinguishing between various cohorts
351 (Supplemental Table S10). Of these, 5 miRNAs were targets which had previously been identified

352 as potentially therapeutic miRNAs[7], and one miRNA, miR-299, was a biomarker which could be
353 collected from plasma which was indicative of cardiac aging.

354 Interestingly, this analysis revealed only 21 potential protein targets for distinguishing between
355 various cohorts (Supplemental Table S10). These were largely identified between young and aged
356 PEVs, and aged TEVs and PEVs (Supplemental Figure S10).

357 ***Treatment of Cardiac Cells with Therapeutic miRNAs Ameliorates Damage Under MI-like***
358 ***Conditions***: Of the potentially therapeutic miRNA targets identified, three (miR-199a, miR-30d,
359 miR-302a) were selected for testing with previously identified therapeutic miRNAs[7]. These
360 miRNAs were encapsulated at 40 nM concentration in lecithin-based lipid nanoparticles (LNPs).
361 The LNPs were ~120 nm in size (Figure 5C), slightly smaller than both TEVs and PEVs, and
362 looked as expected. Hypoxia assays on iCFs and iCMs compared to TEVs and PEVs revealed that
363 miR-loaded LNPs (miR-LNPs) significantly increased iCF survival after hypoxia, comparable to
364 TEVs (Figure 5D), with both showing more than 4-fold increase in living cells compared to the
365 control. A similar, but less significant effect was observed in beating recovery, where TEVs
366 showed a non-significant improvement but miR-LNPs showed a significant improvement
367 compared to the control (Figure 5E). Uptake rate of the EVs was also assessed to determine if the
368 effects were rate or concentration dependent, where TEVs demonstrated a significantly higher
369 uptake rate than PEVs or miR-LNPs (Figure 5F). Furthermore, uptake rate increased over time for
370 both PEVs and TEVs, but remained stagnant for miR-LNPs (Figure 5G).

371

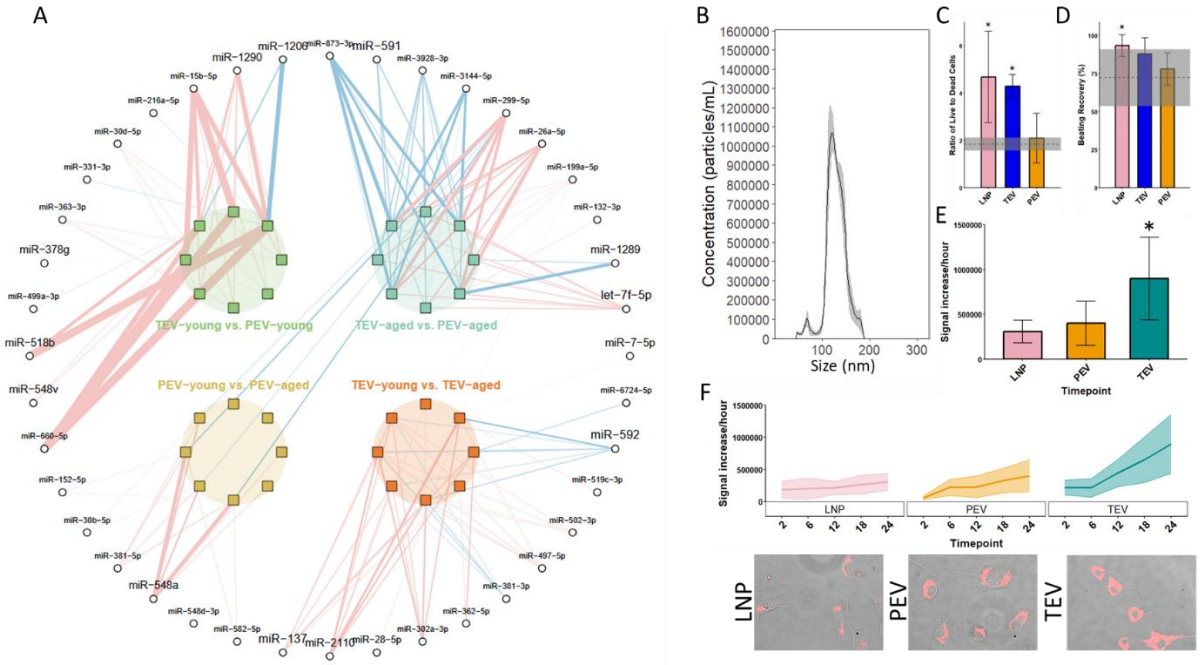

Figure 5. Machine-learning results inform novel theragnostic applications of EV-chaperoned miRNAs. For LNPs, n ≥ 3 in all assays; for TEVs and PEVs, n = 6 biological replicates per cohort, equally spread between male and female donors. A network plot representing the biomarkers selected from eight regularized logistic regression in 4 pairs of cohort comparisons: TEV-young vs. PEV-young; TEV-aged vs. PEV-aged; TEV-young vs. TEV-aged; PEV-young vs. PEV-aged, each depicted by a colored circle at the center of the network (A). The square nodes represent the eight models (with LASSO and SCAD penalties in one full dataset and three biologically defined subsets); the circular nodes along the periphery represent individual miRNA selected by at least one model. Edges connect miRNAs to the models in which they were selected, with red edges indicating a positive coefficient and blue edges indicating a negative coefficient. The thickness of each edge reflects the absolute magnitude of the coefficient. Coefficient heatmaps can be viewed at Supplemental Figure S11.. (C) Nanoparticle Tracking Analysis results for formulated lecithin lipid nanoparticles loaded with therapeutic miRNAs (miR-LNPs). Results for miR-LNP treatment of cells during 2 h hypoxia compared to TEVs and PEVs in CFs (F) and CMs (G). Uptake after 24 h (H) and uptake rate over time (I) for miR-LNPs compared to TEVs and PEVs. * $p < 0.05$.

389 **DISCUSSION**

390 In this study, we isolated and characterized small extracellular vesicles (sEVs) isolated from
391 patient blood plasma samples and from donor heart tissue samples. All sEV samples were taken
392 from an equal number of men (n = 6 for tissue & plasma) and women (n = 6 for tissue and plasma)
393 to minimize the impact of sex variance, and were bifurcated between aged (>50 y.o., n = 6 for
394 tissue & plasma) and young (<40 y.o., n = 6 for tissue & plasma) for analysis (Supplemental Table
395 S1). Both the plasma sEVs (PEVs) and tissue sEVs (TEVs) were observed under transmission
396 electron microscopy (TEM) and population size distribution was assayed via nanoparticle tracking
397 analysis (NTA), with mean and mode population sizes being consistent between both assays.
398 Interestingly, the mode size of the sEV population differed with age in TEVs, but not PEVs,
399 suggesting at least some degree of differential function with respect to aging between each
400 category of EV. Surface protein composition was also assessed between aged and young PEVs
401 and TEVs using western blot for classical exosome markers CD9, CD63, and TSG101[21]. While
402 overall measured expression of these proteins increased with age in TEVs and decreased with age
403 in PEVs, the relative expression of these proteins did not significantly change in either group,
404 suggesting that the quantity, but not overall composition, of tetraspanin web targeting proteins
405 changes with age, and that these changes are different in PEVs and TEVs. Finally, the miRNA and
406 protein content of young and aged PEVs and TEVs were assayed. The miRNA content was
407 measured using Nanostring technology, providing a full profile of human miRNAs, and
408 unsupervised analysis was performed to identify distinguishing miRNAs between PEVs and TEVs
409 which were independent of age. The TEV-specific age-independent miRNAs were further
410 analyzed in MetaCore pathway analysis to provide a preliminary overview of processes uniquely
411 modulated by TEVs. The protein content of all cohorts was similarly assessed using mass

412 spectrometry, revealing 2547 proteins with varying expression levels across all biological
413 replicates. Analysis of the dataset revealed 93 proteins consistently expressed in all biological
414 replicates of all cohorts, with aged sEVs tending to have more commonly expressed proteins than
415 young sEVs and TEVs tending to have more commonly expressed proteins than PEVs. Unique
416 cohort proteins were also identified and assessed for downstream function using KEGG
417 proteomapping software and MetaCore pathway analysis.

418 The size discrepancy in age-related size changes between TEVs and PEVs (Figure 1A, B) is an
419 interesting result due to the known consistency of size distribution in EV populations[21] and our
420 previous study showing that these size differences are also not sex-dependent[7]. We first evaluated
421 whether or not this discrepancy was due to different cell ages in the heart, as the difference due to
422 cell age could have been mitigated in PEVs by the large number of organs which contribute to the
423 PEV population. We evaluated this for both artificially aged iCFs (high passage cells at high
424 confluency) and mCFs from aged mice (72 weeks), but found that neither population showed
425 significantly different EV sizes produced compared to the young cells (Supplemental Figure S1).
426 In previous studies, we have shown that the stiffness of the surrounding matrix can significantly
427 alter the behavior of cells[10,13], so an alternative cause may be differences in the matrix stiffness
428 between young and aged hearts. This discrepancy will be further evaluated in future works to
429 identify the precise relationship, if any, between matrix stiffness and produced EV size.

430 The uptake rate of EVs was also assessed for both populations and revealed novel interactions of
431 TEVs and PEVs with tissue specificity, though only young PEVs and TEVs were used for this
432 assay due to the substantially smaller size of aged TEVs compared to all other cohorts, which we
433 have previously shown increases the uptake rate by cells[7]. To assess the specificity of TEVs and
434 PEVs, uptake was evaluated for both populations with human and non-human (mouse) CFs.

435 Interestingly, the uptake rate for both PEV groups and the non-human uptake of the TEVs was
436 essentially the same at all timepoints measured (Figure 1F) but the uptake of TEVs on human CFs
437 was significantly higher (Figure 1G) and in fact was increasing exponentially by the endpoint
438 (Figure 1F). This suggests some level of specificity of the TEVs that is not present in the PEVs
439 which may distinguish how EVs are selected to be exported to the plasma or to the surrounding
440 ECM. The consistency of tetraspanin expression in TEV populations (Figure 1E) may be a partial
441 contributor to this, as the tetraspanin web has been implicated in EV organ targeting
442 systemically[39–41], with several key, unidentified tetraspanins that are unique to TEVs contributing
443 to the uniqueness of this specificity. Additionally, the exponential increase in rate of uptake of
444 TEVs by human cells suggests that human cells taking up TEVs undergo some change which
445 facilitates further TEV uptake. This has not yet been reported in literature and may be a key aspect
446 of how TEVs provide therapeutic effects in young hearts, as an exponential increase in the uptake
447 of therapeutic compounds over a short period of time would actively counteract increased
448 inflammation and damage-associated effects common in the aftereffects of cardiac insult. These
449 results demand further study, and will be more fully evaluated in future works specifically
450 assessing the dynamics between uptake rate of natural or engineered EVs for the time-sensitive
451 delivery of therapeutic agents.

452 The differential miRNA cargo of TEVs and PEVs provides an interesting avenue for the
453 identification of therapeutic agents, as we have previously established that TEVs, but not PEVs,
454 can promote anti-fibrotic effects in heart cells post-insult[7]. In light of this, the overlap in miRNA
455 expression in the young PEVs and TEVs presents an interesting conundrum, although this is
456 resolved by the nearly bifurcated miRNA expression in the aged EV populations (Figure 2A),
457 suggesting that miRNA cargo substantially diverges between TEVs and PEVs with age. Despite

458 this, it was possible to completely distinguish between TEVs and PEVs as a whole via 125
459 identified miRNAs selected by untargeted analysis of the entire miRNA profile for all cohorts
460 (Figure 2C), providing further evidence that TEVs and PEVs are specialized for different
461 functions. Of the 125 differentiating miRNAs, 59 were enriched in TEVs and 66 were enriched in
462 PEVs, providing ample targets for further analysis of the specific function of each population. To
463 better understand the unique cardiac-related function of the TEVs, we manually assessed the 59
464 TEV-enriched miRNAs for potential involvement in any CVD or CVD-related pathways via
465 public databases and identified 45 targets for downstream analysis. MetaCore pathway analysis of
466 the 45 revealed several pathways which were consistently regulated by several of the target
467 miRNAs (Figure 3E-H). These combined effects served to inhibit targets in the HNF4-α pathway,
468 Smad3/STAT5 pathway, and PPARγ pathway, and promote a therapeutic SDF-1α pathway. These
469 results imply several exciting possibilities. First, we have previously hypothesized the cooperative
470 effects of TEV miRNAs in promoting cardioprotective effects via synergistic inhibition of CVD-
471 associated pathways[7], but were only able to demonstrate this with 4 identified target miRNAs. The
472 combined regulation of 3 damage associated pathways at multiple points by 45 target miRNAs
473 provides a plethora of additional targets to evaluate in order to generate a TEV-mimetic cocktail
474 of beneficial miRNAs for therapeutic applications. The use of a large number of miRNAs which
475 endogenously cooperate to act on a small number of pathways would be able to provide much
476 greater effect specificity than existing single-target drugs and previously proposed single-miRNA
477 therapeutics. Additionally, these miRNAs together not only inhibit damage-associated effects but
478 also promote reparative signaling. The SDF-1α is a known cardioprotective pathway which is
479 difficult to activate without off-target effects. While the utility of these specific miRNAs requires

480 additional study to determine efficacy and viability, this is an exciting first step in the development
481 of highly specific therapeutics using endogenous agents.

482 The protein cargo of both EV populations also provided exciting results. While comparison of all
483 identified proteins separated PEVs and TEVs, this result was not consistent across all biological
484 replicates (Supplemental Figure S7). This was likely due to the inconsistency of protein expression
485 across biological replicates (Figure 2D), with >60% of proteins being expressed in some, but not
486 all, biological replicates of a given cohort. To be consistent in our analysis, we focused on proteins
487 which were either expressed consistently in all cohorts (Figure 2E), or were uniquely expressed in
488 a single cohort (Supplemental Table S8), although cohort-unique targets were still expressed in all
489 biological replicates of a given cohort. Of the proteins consistently expressed in all cohorts, aged
490 EVs tended to express more proteins overall for both TEVs and PEVs (Figure 2F), which is
491 consistent with our previous hypothesis[7]. This suggests that overall proteins included in both
492 systemic and tissue-resident increases with increasing age, which is consistent with the expected
493 effects of inflammaging. Inflammaging has been identified as a potential cause of many aging-
494 related pathologies, but is poorly defined and not well understood. The evaluation of EVs as part
495 of aging-related increases in inflammation may provide a novel avenue for increased
496 understanding of inflammaging and the development of intervention strategies.

497 Analysis of the proteins uniquely expressed in TEVs or PEVs via gene ontology and KEGG
498 proteomapping revealed highly different functions of each population. PEVs were largely involved
499 in immune system regulation (Figure 4B, 4C, Supplemental Figure S9), while TEVs were involved
500 in a host of metabolic and regulatory functions in the heart (Figure 4A, 4C, Supplemental Figure
501 S9). Interestingly, only TEVs were involved in disease progression (Figure 4C). To evaluate the
502 aging-related changes in protein expression, the proteins unique to aged TEVs and PEVs were also

503 mapped (Figure 4C). Again, PEVs were largely involved with the immune system, though immune
504 system interactions made up a much larger proportion of involved pathways than PEVs overall,
505 and now showed involvement with the onset of Alzheimer's Disease pathways, which was an
506 interesting pathway to remain consistent across all biological replicates. TEVs, however, showed
507 much greater involvement in metabolism-related activities, less regulation of cardiac homeostasis,
508 and new involvement in local inflammation and the direct onset of CVDs, differentiating aged
509 TEVs from overall TEVs by direct implication in increased inflammation and disease progression.
510 From the proteins uniquely expressed in TEVs or PEVs overall, 17 proteins of interest were
511 identified which may be involved in the onset and progression of CVD. MetaCore analysis of these
512 proteins revealed mulit-point involvement in three pathways which, while not directly implicated
513 in CVD, are closely linked to the onset of several CVDs. These pathways included
514 NFkB/Interleukin signaling downstream of c-Jun and TRAF6, PI3k-1a, mTOR, and Laminin
515 response, which are each critical to regulating cardiac homeostasis and normal function. In
516 particular, PI3k-1a and mTOR together are a regulatory pathway that is increasingly dysregulated
517 with age, leading to increased risk of CVD, fibrosis, and heart failure[86,87], while the dysregulation
518 of Interleukin signaling and Laminin response pathways are closely related to the onset of chronic
519 fibrosis and other pathological cardiac matrix remodeling [79–85]. This data suggests that these
520 pathways are, in some part, regulated by TEV signaling and that aging-related changes in TEV
521 signaling, such as those we have shown, may disrupt these vital pathways and lead to increased
522 risk of CVD. While more direct evaluation of the roles of TEVs on the regulation of these pathways
523 is essential for understanding the complex relationship of aging-related EV changes and aging-
524 related pathologies, this data provides a first step into understanding these processes.

525 Lastly, using the machine learning-based analyses we were able to validate several hypothesized
526 therapeutic agents from our previous dataset[91]. In particular, miR-199a, which we had considered
527 a significant agent in the initial therapeutic miRNA cocktail, was found to be enriched in young
528 tissue, as we previously observed, and was identified by the analysis, in addition to miR-30d and
529 miR-302a, which had been both identified as targets of interest (Figure 5A). To evaluate the
530 therapeutic potential of these therapeutic miRNAs utilizing a drug delivery vehicle, the miRNAs
531 were mixed at 40 nM and encapsulated in simple lecithin lipid nanoparticles (LNPs) (Figure 5B).
532 While this miR-LNP treatment did significantly increase cell survival and recovery of function
533 post-MI (Figure 5C, 5D), this function appeared to be rate-independent, as the uptake rate of LNPs
534 was lower than both TEVs and PEVs yet the effect on cells was greater in both assays (Figure 5E,
535 5F). While the therapeutic cocktail will need additional formulation and testing, this is a promising
536 early result for the development of a novel, endogenous anti-fibrotic therapy.

537 Overall, this study serves as an in-depth, comprehensive resource for identifying the cargo of sEVs
538 isolated from plasma or cardiac tissue, as well as distinguishing between samples from young or
539 aged individuals. These specific delineations are currently not well documented in literature, and
540 increased assessment and validation of age-related and organ-specific paracrine signaling
541 mechanisms will be essential in the development of next-generation therapeutics. Furthermore,
542 these data suggest that, with increased understanding of both TEV and PEV interactions, it will be
543 possible to closely investigate organ-specific health markers via plasma assays, one of the chief
544 overall goals of biomarker research. The combination of novel machine learning and
545 bioengineering approaches provides a unique avenue to achieve this goal in both a cost-efficient
546 and broadly applicable manner for both other CVDs and other organs altogether. Finally, we
547 demonstrate the feasibility of identifying novel, endogenous therapeutic agents by investigating

548 the age-specific differences in TEV cargo, which we suggested in a previous publication[91] The
549 success of these novel therapeutics in ameliorating damage from MI-like conditions in cardiac
550 cells opens the door to a new class of highly specific therapeutics which take advantage of
551 endogenous repair machinery in the heart.

552 **MATERIALS & METHODS**

553 ***Human Heart Tissue Preparation:*** Donor human heart tissue was prepared according to our
554 previous protocol[7]. Briefly, the left ventricle from frozen heart tissue was excised of fat and
555 connective tissue and section into sub-300 µm slices, which were agitated in an aqueous acetic
556 acid (0.1%, Sigma Aldrich, USA) and ethanol (4%, Sigma Aldrich, USA) solution at 200 rpm at
557 room temperature (RT) for 2 hours. Tissues were then washed in sterile PBS for at least 30 minutes
558 to remove free debris, then re-agitated in solution overnight at RT. Matrices were then vigorously
559 washed in sterile PBS and sterile DI water, lyophilized, pulverized with pre-chilled mortar and
560 pestle, and separated into 200 mg (dry weight) powder aliquots. ECM powder was resuspended in
561 1 mL of aqueous Collagenase Type II (0.2 mg/mL, Corning, USA), Tris buffer (50 mM, Sigma
562 Aldrich, USA), and $CaCl_2$ (5 mM, Amresco, USA) and mixed vigorously. Suspension was reacted
563 overnight at RT with re-mixing every 6 h to prevent settling.

564 ***Plasma Sample Collection:*** Whole blood was collected from patients via direct veinous puncture
565 into ethylenediaminetetraacetic acid (EDTA)-treated tubes to prevent coagulation. Following
566 collection, whole blood was centrifuged at 1000g and 4°C for 5 min to separate plasma. Patient
567 plasma was then aliquoted to sterile RNAse-free tubes and shipped from the University of Florida
568 College of Medicine to the University of Notre Dame at -80°C. After arrival, samples were stored
569 at -80°C until use.

570 ***Vesicle Extraction and Isolation:*** For both digested heart tissue ECM and collected plasma
571 samples, the solution was centrifuged three times at 500g for 10 minutes, 2500g for 20 minutes,
572 and 10,000g for 30 minutes. The pellet was discarded after each centrifugation to remove any
573 insoluble contaminants. After the final centrifugation, the collected supernatant was
574 ultracentrifuged at 100,000g for 70 minutes at 4°C using an ultracentrifuge (Optima MAX-XP
575 Tabletop Ultracentrifuge, Beckman Coulter). The resulting pellet from ultracentrifugation was
576 either used immediately or stored dry at -80°C.

577 ***Transmission Electron Microscopy:*** Single pellets were fixed via resuspension in 2.5%
578 glutaraldehyde solution for 2 h at RT in the dark. Fixed samples were then loaded onto plasma-
579 cleaned Formvar/carbon-coated copper 200 mesh grids (Polysciences) and negative-stained with
580 Vanadium staining solution (Abcam, ab172780). The resulting grids were imaged at 80 kV with a
581 TEM (JEOL 2011, Japan).

582 ***Nanoparticle Tracking Analysis:*** Single pellets were resuspended in 500 µL of sterile, particle-
583 free PBS and measured using a NanoSight NS300 machine (Malvern Panalytical) with NTA
584 software version 3.2.16. Resuspended samples were kept at 4 °C until measurement, and
585 measurements were taken at RT.

586 ***Western Blot:*** Single pellets were lysed in RIPA buffer containing 1% proteinase inhibitor cocktail
587 (Brand, Country) at 4°C for 30 minutes and resultant protein concentration was measured via
588 bicinchoninic acid (BCA) assay (Pierce Chemical). Equal amounts of protein for each sample were
589 separated by 12% SDS-PAGE and transferred to blotting membranes. Blotting membranes were
590 incubated on a rocker overnight at 4°C with rabbit polyclonal primary antibodies against CD9
591 (Abcam, ab223052), CD63 (Abcam, ab216130), and TSG101 (Abcam, ab30871) at (1:1000), then
592 for 1 h at RT with HRP-conjugated goat anti-rabbit secondary antibody (Abcam, ab205718).

593 Stained membranes were then treated with a chemiluminescent substrate (Clarity ECL, Bio-Rad)
594 and imaged using a ChemiDoc-It2 imager (UVP, Analytik Jena) equipped with VisionWorks
595 software. Images were processed using ImageJ (NIH).

596 ***Culture of Human Induced Pluripotent Stem Cells (hiPSCs)***: DiPS 1016 SevA hiPSCs, which
597 were derived from human skin fibroblasts, were cultured on Geltrex (1% Invitrogen, USA)-coated
598 culture flasks in mTeSR (StemCell Technologies, Canada) media supplemented with 1% penicillin
599 (VWR, USA) under standard culture conditions from passages 40-50.

600 Cells were passaged at 80% confluency. To passage the hiPSCs, cells were detached using
601 Accutase (StemCell Technologies, Canada) and seeded onto Geltrex-coated cell culture well plates
602 or split between cell culture flasks. Seeding was performed in mTeSR media supplemented with
603 Rho-associated, coiled-coil containing protein kinase (ROCK) inhibitor (5 μM, StemCell
604 Technologies, Canada). For differentiation, cells were cultured until 95% confluency before
605 starting a protocol

606 ***Differentiation and Culture of hiPSC-derived Cardiac Fibroblasts (iCFs)***: In-house
607 differentiated induced pluripotent stem cell (iPSC)-derived cardiac fibroblasts (iCFs) were
608 generated and cultured according to our previous protocol[13], and were seeded on fibronectin (50
609 μL/mL) -coated 24-well cell culture plates. Mouse primary cardiac fibroblasts were isolated from
610 collected mouse hearts according to our previous protocol[7], and were seeded on fibronectin-coated
611 24-well cell culture plates as with iCFs. Both iCFs and mCFs were cultured in Dulbecco's
612 Modified Eagle's Medium (DMEM, Thermo Fisher, USA), supplemented with fetal bovine serum
613 (FBS, 10%, Gibco, USA), penicillin/streptomycin antibiotics (P/S, 1%, Life Technologies, USA),
614 and SD208 (3 μM, Sigma Aldrich, USA).

615 ***Culture of Mouse Primary Cardiac Fibroblasts (mCFs)***: Isolated mCFs were seeded on
616 fibronectin-coated 24-well cell culture plates as with iCFs. Both iCFs and mCFs were cultured in
617 Dulbecco's Modified Eagle's Medium (DMEM, Thermo Fisher, USA), supplemented with fetal
618 bovine serum (FBS, 10%, Gibco, USA), penicillin/streptomycin antibiotics (P/S, 1%, Life
619 Technologies, USA), and SD208 (3 μM, Sigma Aldrich, USA).

620 ***Cellular Uptake of sEVs:*** Cellular uptake of sEVs was performed based on our previous protocol[7].
621 Briefly, sEV pellets were resuspending in PBS and concentration was assessed via BCA assay and
622 subsequently stained using the ExoGlow-Membrane staining kit (System Biosciences, USA) for
623 30 min at RT. Stained sEVs or a blank control were then purified in a salt gradient column for a
624 final sEV concentration of 25 μg/mL in DMEM, supplemented with exosome-free FBS (10%) and
625 1% P/S. Cells were incubated with the sEV-conditioned media at 37°C and imaged at 0, 3, 8, 16,
626 and 24 h incubation. During imaging the conditioned media was exchanged with sterile, particle-
627 free PBS, and the same media was re-placed in the same wells immediately preceding return to
628 incubation.

629 ***miRNA Isolation:*** Internal RNAs were isolated from sEVs using the Total Exosome RNA &
630 Protein Isolation Kit (Thermo Fisher Scientific, USA) according to the manufacturer's protocol.
631 Briefly, single pellets were resuspended in sterile, particle-free PBS and incubated with an equal
632 volume of provided denaturation buffer 4 °C for 5 min. The solution was then mixed with an equal
633 volume of Acid-Phenol:Chloroform by vortexing for 30 seconds and centrifuged for 5 min at
634 15,000g. The resulting aqueous phase was extracted and combined with 1.25x volume of 100%
635 ethanol, then transferred to the provided spin column. The spin column was centrifuged at 10,000g
636 for 15 seconds to bind and wash the RNA, then the RNA was eluted in 100 μL of the provided
637 elution solution. Eluted RNA was then concentrated using 3 kDa microcentrifuge spin filters

638 (Amicon, USA). 100 µL miRNA solution was worked up to 420 µL with RNAse-free water and
639 placed into a filter, then centrifuged at 14,000g for 90 minutes. Next, the filter was inverted into a
640 fresh collection tube, and centrifuged at 8,000g for 2 minutes. The resulting 20-25 µL of RNA
641 concentrate was immediately quantified by microvolume spectrophotometery (Nanodrop 2000,
642 Thermo Fisher Scientific, USA).

643 ***Profiling of Total miRNA Population:*** Concentrated RNA isolate was prepared for Nanostring
644 miRNA profiling according to the manufacturer's protocol. Briefly, the provided miRNA codeset
645 was mixed with the provided hybridization buffer to produce a master mix, and spike-in miRNA
646 controls were prepared at 200 pm. In order, the master mix, concentrated sample miRNA, spike-
647 in miRNA, and provided probes were mixed in a PCR plate and incubated at 65 °C for 16 h. The
648 hybridized solution was then mixed with 15 µL of provided hybridization buffer, for a total volume
649 of 30-35 µL, and added to the provided microfluidic cartridge. The assay was run with the provided
650 protocol for total miRNA analysis, and data was processed and analyzed using the provided
651 software using the recommended settings. The dataset was then exported for further analysis and
652 target selection.

653 ***miRNA Gene Target Identification and Gene Ontology:*** Likely gene targets of miRNAs were
654 predicted by miRDB[92], miRTarBase[93], and TargetScan[94], and commonly predicted genes were
655 compiled for further analysis (Supplemental Table S5). In-house software was used to identify
656 unique genes and match miRNAs to the corresponding gene targets to determine overlapping gene
657 targets between miRNAs of interest. Gene targets were selected as genes which were predicted
658 targets for greater than or equal to 10 miRNA targets (Supplemental Table S6).

659 Gene Ontology Analysis (GOA) was performed on the identified gene targets using an online
660 database via PANTHER Gene Ontology classification for enrichment analysis[95–97]. Data was
661 extracted from the output and graphed using R.

662 ***miRNA Pathway Analysis:*** Exported Nanostring data was normalized via Log10 normalization
663 and uploaded to the Clarivate MetaCore system for pathway analysis, then cleaned to remove
664 erroneous miRNA detection, if any, by the system. Automated network analysis was conducted
665 with 50 nodes per network. Results were presented as pathways obtained from the software.

666 ***Protein Isolation:*** Single pellets were lysed in 1% Triton-X solution at 4°C overnight, and
667 resultant protein concentration was measured via bicinchoninic acid (BCA) assay (Pierce
668 Chemical, USA). The resulting protein solution was solubilized in an SDS buffer solution
669 consisting of 5% SDS, 50 nM TEAB (pH 7.55) at room temperature until fully combined.

670 ***Total Protein Profiling:*** Total protein profiling was performed via mass spectrometery (Q
671 Exactive HF Mass Spectrometer) according to the manufacturer's protocol. Briefly, solubilized
672 protein samples were denatured in 20 mM DTT, then alkylated with 40 mM iodoacetamide.
673 Alkylated samples were digested in a provided column with trypsin (1:25 wt:wt) in 50 mM TEAB
674 (pH 8) at 37°C overnight. Digested samples were then desalted via ziptip C18 and dried, then
675 reconstituted in acetonitrile. Mass spectrometry was run with 1 µL of acetonitrile-reconstituted
676 solution for bottom-up proteomics.

677 ***Protein pathway mapping:*** GOA was performed on enriched proteins using the same protocol as
678 described above. Data was extracted from the output dataset and graphed using R. Proteomic
679 interactions of uniquely enriched proteins were classified through KEGG-based proteomapping
680 software[98] and are presented as obtained.

681 ***Machine Learning-Based Analysis***: The datasets analyzed consisted of four cohorts: TEV-young
682 (n=6), TEV-aged (n=6), PEV-young (n=6), and PEV-aged (n=6) for the analysis of 798 identified
683 miRNAs; TEV-young (n=6), TEV-aged (n=6), PEV-young (n=6), and PEV-aged (n=6) for the
684 analysis of 2547 identified proteins. Regularized logistic regression was used to identify
685 biomarkers potentially associated with cohort differences. Comparisons were performed between
686 young (TEV-young vs. PEV-young), aged (TEV-aged vs. PEV-aged), TEV (TEV-young vs. TEV-
687 aged), and PEV (PEV-young vs. PEV-aged) groups.

688 The negative log-likelihood function for the logistic regression is:

689 $$l(\beta_0, \boldsymbol{\beta}) = -\sum_{i=1}^{n}\{y_i \ln(\pi_i) + (1 - y_i)\ln(\pi_i)\}, \qquad \text{(Equation 1)}$$

690 where the log-odds are

691 $$\ln\left(\frac{\pi_i}{1-\pi_i}\right) = \beta_0 + \sum_{j=1}^{p} x_{ij}\beta_j, \qquad \text{(Equation 2)}$$

692 for $i = 1, 2, \ldots, n$, and $\boldsymbol{x}_i$ is a $p \times 1$ vector that contains the values of p miRNA biomarkers in
693 sample i, and $y_i \in \{0, 1\}$ is a binary group indicator. β_0 is the intercept and $\boldsymbol{\beta} = (\beta_1, \beta_2, \ldots \beta_p)$ is a
694 $p \times 1$ vector of regression coefficients. To perform variable selection, a penalty term was added
695 to the likelihood:

696 $$-\sum_{i=1}^{n}\{y_i \ln(\pi_i) + (1 - y_i)\ln(\pi_i)\} + \lambda P(\boldsymbol{\beta}), \qquad \text{(Equation 3)}$$

697 where the penalty term $\lambda P(\boldsymbol{\beta})$ represents the product of tuning parameter λ and the penalty function
698 $P(\boldsymbol{\beta})$. Penalized regression is often used for variable selection and regularizing parameter
699 estimation and predictions when p is large, especially when n is small, so as to improve the
700 robustness and generalizability of the learned model.

701 Two widely adopted penalty functions were applied: LASSO (least absolute shrinkage and selector
702 operation)[99] and SCAD (smoothly clipped absolute deviation)[100]. The penalty functions are
703 defined as:

704 $$P(\boldsymbol{\beta}) = \begin{cases} \sum_{j=1}^{p} |\beta_j| & \text{LASSO} \\ \sum_{j=1}^{p} \lambda|\beta_j| I(|\beta_j| \le \lambda) - \frac{|\beta_j|^2 - 2a\lambda|\beta_j| + \lambda^2}{2(a-1)} I(\lambda < |\beta_j| \le a\lambda) + \frac{(a+1)\lambda^2}{2} I(|\beta_j| > \lambda) & \text{SCAD} \end{cases} \quad \text{(Equation 4)}$$

705 The tuning parameter λ was selected via the leave-one-out cross validation (LOOCV).

706 In addition to running the above logistic regression models with LASSO and SCAD penalties on
707 the full datasets (798 miRNAs, 2547 proteins), the analyses were also performed on biologically
708 informed subsets. The miRNA dataset was divided into 3 subsets: (1) purely cardiac specific
709 miRNAs (450); (2) cardiac specific and vasculature miRNAs (565); (3) cardiac specific,
710 vasculature, cerebral vasculature, and rare cardiac disease miRNAs (576) – leading to 8 models in
711 total for each comparison. For the protein dataset, subsets were created based on proteins with
712 non-zero values across all biological replicates in a given comparison (young: 127, aged: 220,
713 tissue: 209, plasma: 225). Targets were selected from biomarkers identified in the subsetted
714 analysis.

715 All analyses were performed in R. For LASSO regression, R package "glmnet v4.1-8" was used;
716 for SCAD, R package "ncvreg v3.14.3" was employed.

717 Regarding the coefficient interpretation, each logistic regression model uses a binary variable to
718 indicate group membership, where the reference group is coded as 0 (e.g., **aged** or **TEV**), and the
719 comparison group is coded as 1 (e.g., **young** or **PEV**). The model estimates the log-odds of
720 belonging to the comparison group based on the expression levels of selected biomarkers. A
721 **positive coefficient** implies that increased expression of the biomarker is associated with higher

722 odds of being in the comparison group (e.g., young or PEV), whereas a **negative coefficient**
723 indicates that the biomarker is more strongly associated with the reference group (e.g., aged or
724 TEV).

725 ***Lipid Nanoparticle (LNP) Formation and miRNA Encapsulation***: Lipid nanoparticles (LNPs)
726 formed from lecithin (soy, Neogen), an inexpensive and benign lipid[101] of recent interest in
727 synthesis of LNPs from naturally occurring lipids[102], particularly for cardiac drug delivery[103], were
728 formed by simple hot extrusion. Briefly, mixed into PBS at 3 mM concentration and heated to
729 50°C while mixing to form a lipid emulsion. This temperature is sufficient for lecithin mixing into
730 water for LNP formation[104] and low enough to avoid denaturing miRNAs during lipid nanoparticle
731 (LNP) formation[105]. Once lecithin is sufficiently mixed, miRNA mimics were added to the solution
732 for final concentration of 40 nM total miRNAs. The miRNA mimics added were miR-199a
733 (ACAGUAGUCUGCACAUUGGUUA, miRVana), miR-30d
734 (UGUAAACAUCCCCGACUGGAAG, miRVana), miR-302a
735 (ACUUAAACGUGGAUGUACUUGCU, miRVana) miR-125
736 (ACGGGUUAGGCUCUUGGGAGCU, miRVana), miR-143
737 (UGAGAUGAAGCACUGUAGCUC, miRVana), and miR-222
738 (AGCUACAUCUGGCUACUGGGU, miRVana). Once the miRNAs were added, the lipid-miR
739 mixture was hot extruded[106] while cooling, through a 100 nm membrane to generate LNPs with
740 miRNAs encapsulated (miR-LNPs). This was done using a Mini-Extruder (Avanti Polar Lipids)
741 and corresponding membrane.

742 ***Hypoxia Assay***: To analyze the contractility of iCMs, a block-matching algorithm was performed
743 using MATLAB as described previously[107]. Briefly, iCM or 3D structures were recorded in
744 brightfield in real time under a microscope (Axio Observer. Z1, Zeiss, Hamamatsu C11440 digital

745 camera) for 30 s intervals. Videos were then uploaded to the analysis software, and beating velocity
746 and frequency were calculated, and contraction heat maps were plotted. Baseline beating rates of
747 iCMs were measured before beginning the hypoxia assay.

748 iCFs or iCMs were transferred to deoxygenated (>12 h hypoxia) media containing 1 milliong
749 particle/mL LNPs with or without miRNA encapsulation (miR-LNP and control, respectively), or
750 TEV or PEVs at 25 μg/mL as measured by bicinchoninic acid (BCA) assay (Pierce Chemical).
751 Cell were then subjected to hypoxia for 3 hours, which we have previously shown is sufficient to
752 induce MI-like cell death[6]. Following hypoxia, iCF plates were stained with calcein AM and
753 ethidium homodimer-1 Live/Dead stains (Invitrogen, 1:1000) to quantify living and dead cells,
754 respectively. Stained cells were imaged, and images were quantified in ImageJ.

755 To analyze the contractility of iCMs, a block-matching algorithm was performed using MATLAB
756 as described previously[107]. Briefly, iCM or 3D structures were recorded in brightfield in real time
757 under a microscope (Axio Observer. Z1, Zeiss, Hamamatsu C11440 digital camera) for 30 s
758 intervals. Videos were then uploaded to the analysis software, and beating velocity and frequency
759 were calculated, and contraction heat maps were plotted, and % recovery was calculated relative
760 to the control. Timepoints were taken every 12 h following the removal of the iCMs from hypoxia.

761 **Statistical Analysis:** Results were analyzed by one-way analysis of variance (ANOVA) with post-
762 hoc Tukey's HSD, two-way ANOVA with post-hoc Tukey's multiple comparison test, or a two-
763 tailed Welch t-test for unequal standard deviation. Values are presented as the mean ± standard
764 deviation (SD) unless otherwise indicated, and differences were considered significant when $p \leq$
765 0.05.

766 **List of Supplementary Materials:**

767 Fig S1 to S10

768 Table S1 to S10

769 **REFERENCES**

770 1. Rahimi, K., Duncan, M., Pitcher, A., Emdin, C. A. & Goldacre, M. J. Mortality from heart failure,
771 acute myocardial infarction and other ischaemic heart disease in England and Oxford: a trend
772 study of multiple-cause-coded death certification. *J Epidemiol Community Health* **69**, 1000–1005
773 (2015).

774 2. Reyes-Farias, M., Fos-Domenech, J., Serra, D., Herrero, L. & Sánchez-Infantes, D. White adipose
775 tissue dysfunction in obesity and aging. *Biochem Pharmacol* **192**, 114723 (2021).

776 3. Laconi, E., Marongiu, F. & DeGregori, J. Cancer as a disease of old age: changing mutational and
777 microenvironmental landscapes. *British Journal of Cancer 2020 122:7* **122**, 943–952 (2020).

778 4. Xi, J. Y., Lin, X. & Hao, Y. T. Measurement and projection of the burden of disease attributable to
779 population aging in 188 countries, 1990-2050: A population-based study. *J Glob Health* **12**,
780 (2022).

781 5. Population Reference Bureau (PRB). Countries With the Oldest Populations in the World.
782 https://www.prb.org/resources/countries-with-the-oldest-populations-in-the-world/ (2020).

783 6. Ozcebe, S. G., Bahcecioglu, G., Yue, X. S. & Zorlutuna, P. Effect of cellular and ECM aging on
784 human iPSC-derived cardiomyocyte performance, maturity and senescence. *Biomaterials* **268**,
785 120554 (2021).

786 7. Ronan, G., Bahcecioglu, G., Yang, J. & Zorlutuna, P. Age and Sex-Dependent Differences in Human
787 Cardiac Matrix-Bound Exosomes Modulate Fibrosis through Synergistic miRNA Effects. *bioRxiv*
788 2022.11.14.516464 (2022) doi:10.1101/2022.11.14.516464.

789 8. Ozcebe, S. G. & Zorlutuna, P. In need of age-appropriate cardiac models: Impact of cell age on
790 extracellular matrix therapy outcomes. *Aging Cell* **22**, e13966 (2023).

791 9. Basara, G. *et al.* Myocardial infarction from a tissue engineering and regenerative medicine point
792 of view: A comprehensive review on models and treatments. *Biophys Rev* **3**, 031305 (2022).

793 10. Basara, G., Gulberk Ozcebe, S., Ellis, B. W. & Zorlutuna, P. Tunable Human Myocardium Derived
794 Decellularized Extracellular Matrix for 3D Bioprinting and Cardiac Tissue Engineering. *Gels 2021,*
795 *Vol. 7, Page 70* **7**, 70 (2021).

796 11. Yang, J., Bahcecioglu, G. & Zorlutuna, P. The Extracellular Matrix and Vesicles Modulate the
797 Breast Tumor Microenvironment. *Bioengineering (Basel)* **7**, (2020).

798 12. Ellis, B. W. *et al.* Adipose Stem Cell Secretome Markedly Improves Rodent Heart and hiPSC-
799 derived Cardiomyocyte Recovery from Cardioplegic Transport Solution Exposure. *Stem Cells* **39**,
800 170 (2021).

801 13. Basara, G., Celebi, L. E., Ronan, G., Discua Santos, V. & Zorlutuna, P. 3D bioprinted aged human
802 post-infarct myocardium tissue model. *Health Sci Rep* **7**, e1945 (2024).

803 14. Ozcebe, S. G., Tristan, M. & Zorlutuna, P. Adult Human Heart ECM Improves Human iPSC-CM
804 Function via Mitochondrial and Metabolic Maturation. *bioRxiv* 2023.10.31.565062 (2023)
805 doi:10.1101/2023.10.31.565062.

806 15. Ellis, B. W. *et al.* Human Heart Anoxia and Reperfusion Tissue (HEART) Model for the Rapid Study
807 of Exosome Bound miRNA Expression As Biomarkers for Myocardial Infarction. *Small* **18**, 2201330
808 (2022).

809 16. Ellis, B. W., Acun, A., Isik Can, U. & Zorlutuna, P. Human iPSC-derived myocardium-on-chip with
810 capillary-like flow for personalized medicine. *Biomicrofluidics* **11**, 024105 (2017).

811 17. Ronan, G., Bahcecioglu, G., Aliyev, N. & Zorlutuna, P. Engineering the cardiac tissue
812 microenvironment. *Progress in Biomedical Engineering* **6**, 012002 (2023).

813 18. D'Anca, M. *et al.* Exosome Determinants of Physiological Aging and Age-Related
814 Neurodegenerative Diseases. *Front Aging Neurosci* **11**, 232 (2019).

815 19. Eitan, E. *et al.* Age-Related Changes in Plasma Extracellular Vesicle Characteristics and
816 Internalization by Leukocytes. *Sci Rep* **7**, 1342 (2017).

817 20. Sheta, M., Taha, E. A., Lu, Y. & Eguchi, T. Extracellular Vesicles: New Classification and Tumor
818 Immunosuppression. *Biology (Basel)* **12**, (2023).

819 21. Welsh, J. A. *et al.* Minimal information for studies of extracellular vesicles (MISEV2023): From
820 basic to advanced approaches. *J Extracell Vesicles* **13**, e12404 (2024).

821 22. Xu, M. Y., Ye, Z. S., Song, X. T. & Huang, R. C. Differences in the cargos and functions of exosomes
822 derived from six cardiac cell types: a systematic review. *Stem Cell Res Ther* **10**, 194 (2019).

823 23. Yáñez-Mó, M. *et al.* Biological properties of extracellular vesicles and their physiological
824 functions. *J Extracell Vesicles* **4**, 27066 (2015).

825 24. Jia, Y. *et al.* Small extracellular vesicles isolation and separation: Current techniques, pending
826 questions and clinical applications. *Theranostics* **12**, 6548 (2022).

827 25. Huang, K. *et al.* An off-the-shelf artificial cardiac patch improves cardiac repair after myocardial
828 infarction in rats and pigs. *Sci Transl Med* **12**, (2020).

829 26. Ren, X. *et al.* A multiplexed ion-exchange membrane-based miRNA (MIX·miR) detection platform
830 for rapid diagnosis of myocardial infarction. *Lab Chip* **21**, 3876–3887 (2021).

831 27. Bahcecioglu, G. *et al.* Aged Breast Extracellular Matrix Drives Mammary Epithelial Cells to an
832 Invasive and Cancer-Like Phenotype. *bioRxiv* 2020.09.30.320960 (2020)
833 doi:10.1101/2020.09.30.320960.

834 28. Yang, J., Bahcecioglu, G., Ronan, G. & Zorlutuna, P. Aged breast matrix bound vesicles promote
835 breast cancer invasiveness. *Biomaterials* **306**, 122493 (2024).

836 29. Basara, G. *et al.* Electrically conductive 3D printed Ti3C2Tx MXene-PEG composite constructs for
837 cardiac tissue engineering. *Acta Biomater* **139**, 179 (2022).

838 30. Law, M. R., Watt, H. C. & Wald, N. J. The underlying risk of death after myocardial infarction in
839 the absence of treatment. *Arch Intern Med* **162**, 2405–2410 (2002).

840 31. Cupples, L. A., Gagnon, D. R., Wong, N. D., Ostfeld, A. M. & Kannel, W. B. Preexisting
841 cardiovascular conditions and long-term prognosis after initial myocardial infarction: The
842 Framingham Study. *Am Heart J* **125**, 863–872 (1993).

843 32. Narins, C. R. *et al.* Relationship Between Intermittent Claudication, Inflammation, Thrombosis,
844 and Recurrent Cardiac Events Among Survivors of Myocardial Infarction. *Arch Intern Med* **164**,
845 440–446 (2004).

846 33. Zhu, J. *et al.* The incidence of acute myocardial infarction in relation to overweight and obesity: a
847 meta-analysis. *Arch Med Sci* **10**, 855 (2014).

848 34. Yusuf, S. *et al.* Effect of potentially modifiable risk factors associated with myocardial infarction in
849 52 countries (the INTERHEART study): case-control study. *Lancet* **364**, 937–952 (2004).

850 35. Florio, M. C., Magenta, A., Beji, S., Lakatta, E. G. & Capogrossi, M. C. Aging, MicroRNAs, and Heart
851 Failure. *Curr Probl Cardiol* **45**, 100406 (2020).

852 36. Anand, S. S. *et al.* Risk factors for myocardial infarction in women and men: insights from the
853 INTERHEART study. *Eur Heart J* **29**, 932–940 (2008).

854 37. Piccinini, A. M. & Midwood, K. S. Illustrating the interplay between the extracellular matrix and
855 microRNAs. *Int J Exp Pathol* **95**, 158–180 (2014).

856 38. Huleihel, L. *et al.* Matrix-bound nanovesicles within ECM bioscaffolds. *Sci Adv* **2**, (2016).

857 39. Smith, Z. J. *et al.* Single exosome study reveals subpopulations distributed among cell lines with
858 variability related to membrane content. *J Extracell Vesicles* **4**, 28533 (2015).

859 40. Rana, S., Yue, S., Stadel, D. & Zöller, M. Toward tailored exosomes: The exosomal tetraspanin
860 web contributes to target cell selection. *Int J Biochem Cell Biol* **44**, 1574–1584 (2012).

861 41. Barranco, I. *et al.* Extracellular vesicles isolated from porcine seminal plasma exhibit different
862 tetraspanin expression profiles. *Scientific Reports 2019 9:1* **9**, 1–9 (2019).

863 42. Li, F. *et al.* Zinc Finger Protein ZBTB20 protects against cardiac remodelling post-myocardial
864 infarction via ROS-TNFα/ASK1/JNK pathway regulation. *J Cell Mol Med* **24**, 13383–13396 (2020).

865 43. Corella, D. *et al.* CLOCK gene variation is associated with incidence of type-2 diabetes and
866 cardiovascular diseases in type-2 diabetic subjects: Dietary modulation in the PREDIMED
867 randomized trial. *Cardiovasc Diabetol* **15**, 1–12 (2016).

868 44. Edwards, T. L., Michels, K. A., Hartmann, K. E. & Velez Edwards, D. R. BET1L and TNRC6B associate
869 with uterine fibroid risk among European Americans. *Hum Genet* **132**, 943–953 (2013).

870 45. Bai, Z., Luo, Y. & Tian, L. ERCC5, HES6 and RORA are potential diagnostic markers of coronary
871 artery disease. *FEBS Open Bio* **12**, 1814–1827 (2022).

872 46. Zhang, T. & Ge, J. Mechanism of CREB1 in cardiac function of rats with heart failure via regulating
873 the microRNA-376a-3p/TRAF6 axis. *Mammalian Genome* **33**, 490–501 (2022).

874 47. Wang, C. *et al.* The Effect of Mecp2 on Heart Failure. *Cellular Physiology and Biochemistry* **47**,
875 2380–2387 (2018).

876 48. Bone, W. P. *et al.* Multi-trait association studies discover pleiotropic loci between Alzheimer's
877 disease and cardiometabolic traits. *Alzheimers Res Ther* **13**, 1–14 (2021).

878 49. Fang, C. Y., Lai, T. C., Hsiao, M. & Chang, Y. C. The Diverse Roles of TAO Kinases in Health and
879 Diseases. *International Journal of Molecular Sciences 2020, Vol. 21, Page 7463* **21**, 7463 (2020).

880 50. Song, Y. *et al.* M2 Microglia Extracellular Vesicle miR-124 Regulates Neural Stem Cell
881 Differentiation in Ischemic Stroke via AAK1/NOTCH. *Stroke* **54**, 2629–2639 (2023).

882 51. Xin, X. *et al.* Development and therapeutic potential of adaptor-associated kinase 1 inhibitors in
883 human multifaceted diseases. *Eur J Med Chem* **248**, 115102 (2023).

884 52. Rafiq, K. *et al.* C-Cbl inhibition improves cardiac function and survival in response to myocardial
885 ischemia. *Circulation* **129**, 2031–2043 (2014).

886 53. Tang, Z. *et al.* Suppression of c-Cbl tyrosine phosphorylation inhibits neointimal formation in
887 balloon-injured rat arteries. *Circulation* **118**, 764–772 (2008).

888 54. De Melker, A. A., Van Der Horst, G., Calafat, J., Jansen, H. & Borst, J. c-Cbl ubiquitinates the EGF
889 receptor at the plasma membrane and remains receptor associated throughout the endocytic
890 route. *J Cell Sci* **114**, 2167–2178 (2001).

891 55. Cormont, M. *et al.* CD2AP/CMS Regulates Endosome Morphology and Traffic to the Degradative
892 Pathway Through its Interaction with Rab4 and c-Cbl. *Traffic* **4**, 97–112 (2003).

893 56. Ravandi, A. *et al.* Relationship of IgG and IgM autoantibodies and immune complexes to oxidized
894 LDL with markers of oxidation and inflammation and cardiovascular events: Results from the
895 EPIC-norfolk study. *J Lipid Res* **52**, 1829–1836 (2011).

896 57. Zheng, Y. *et al.* Modulation of STAT3 and STAT5 activity rectifies the imbalance of Th17 and Treg
897 cells in patients with acute coronary syndrome. *Clinical Immunology* **157**, 65–77 (2015).

898 58. Kurdi, M., Zgheib, C. & Booz, G. W. Recent Developments on the Crosstalk Between STAT3 and
899 Inflammation in Heart Function and Disease. *Front Immunol* **9**, 421289 (2018).

900 59. Pang, Q. *et al.* Regulation of the JAK/STAT signaling pathway: The promising targets for
901 cardiovascular disease. *Biochem Pharmacol* **213**, 115587 (2023).

902 60. Liu, J. ; *et al.* The Role of JAK/STAT Pathway in Fibrotic Diseases: Molecular and Cellular
903 Mechanisms. *Biomolecules 2023, Vol. 13, Page 119* **13**, 119 (2023).

904 61. Hanna, A., Humeres, C. & Frangogiannis, N. G. The role of Smad signaling cascades in cardiac
905 fibrosis. *Cell Signal* **77**, 109826 (2021).

906 62. Zhang, M. *et al.* Notch3 Ameliorates Cardiac Fibrosis After Myocardial Infarction by Inhibiting the
907 TGF-β1/Smad3 Pathway. *Cardiovasc Toxicol* **16**, 316–324 (2016).

908 63. Lu, Q. *et al.* Targeting peroxisome proliferator-activated receptors: A new strategy for the
909 treatment of cardiac fibrosis. *Pharmacol Ther* **219**, 107702 (2021).

910 64. Liu, H. J., Liao, H. H., Yang, Z. & Tang, Q. Z. Peroxisome proliferator-activated receptor-γ is critical
911 to cardiac fibrosis. *PPAR Res* **2016**, (2016).

912 65. Li, X. *et al.* Aspirin Reduces Cardiac Interstitial Fibrosis by Inhibiting Erk1/2-Serpine2 and P-Akt
913 Signalling Pathways. *Cellular Physiology and Biochemistry* **45**, 1955–1965 (2018).

914 66. Zhang, Z., Yang, Z., Wang, S., Wang, X. & Mao, J. Targeting MAPK-ERK/JNK pathway: A potential
915 intervention mechanism of myocardial fibrosis in heart failure. *Biomedicine & Pharmacotherapy*
916 **173**, 116413 (2024).

917 67. Mohamad, H. E., Askar, M. E. & Hafez, M. M. Management of cardiac fibrosis in diabetic rats; The
918 role of peroxisome proliferator activated receptor gamma (PPAR-gamma) and calcium channel
919 blockers (CCBs). *Diabetol Metab Syndr* **3**, 1–12 (2011).

920 68. Pillarisetti, K. & Gupta, S. K. Cloning and relative expression analysis of rat stromal cell derived
921 factor-1 (SDF-1)1: SDF-1 α mRNA is selectively induced in rat model of myocardial infarction.
922 *Inflammation* **25**, 293–300 (2001).

923 69. Boyle, A. J. *et al.* Myocardial production and release of MCP-1 and SDF-1 following myocardial
924 infarction: Differences between mice and man. *J Transl Med* **9**, 1–8 (2011).

925 70. Chen, Y. *et al.* Testosterone replacement therapy promotes angiogenesis after acute myocardial
926 infarction by enhancing expression of cytokines HIF-1a, SDF-1a and VEGF. *Eur J Pharmacol* **684**,
927 116–124 (2012).

928 71. Zhong, J. & Rajagopalan, S. Dipeptidyl peptidase-4 regulation of SDF-1/CXCR4 axis: Implications
929 for cardiovascular disease. *Front Immunol* **6**, 159972 (2015).

930 72. Döring, Y., Pawig, L., Weber, C. & Noels, H. The CXCL12/CXCR4 chemokine ligand/receptor axis in
931 cardiovascular disease. *Front Physiol* **5 JUN**, 88349 (2014).

932 73. Wen, J., Zhang, J.-Q., Huang, W. & Wang, Y. SDF-1α and CXCR4 as therapeutic targets in
933 cardiovascular disease. *Am J Cardiovasc Dis* **2**, 20 (2012).

934 74. Fiordelisi, A., Iaccarino, G., Morisco, C., Coscioni, E. & Sorriento, D. NFkappaB is a Key Player in
935 the Crosstalk between Inflammation and Cardiovascular Diseases. *International Journal of*
936 *Molecular Sciences 2019, Vol. 20, Page 1599* **20**, 1599 (2019).

937 75. Cheng, W. *et al.* NF-κB, A Potential Therapeutic Target in Cardiovascular Diseases. *Cardiovascular*
938 *Drugs and Therapy 2022 37:3* **37**, 571–584 (2022).

939 76. Przybyszewski, E. M., Targher, G., Roden, M. & Corey, K. E. Nonalcoholic Fatty Liver Disease and
940 Cardiovascular Disease. *Clin Liver Dis (Hoboken)* **17**, 19–22 (2021).

941 77. Abdullah, M., Berthiaume, J. M. & Willis, M. S. Tumor necrosis factor receptor-associated factor 6
942 as a nuclear factor kappa B-modulating therapeutic target in cardiovascular diseases: at the heart
943 of it all. *Translational Research* **195**, 48–61 (2018).

944 78. Huang, W. *et al.* MicroRNA-3614 regulates inflammatory response via targeting TRAF6-mediated
945 MAPKs and NF-κB signaling in the epicardial adipose tissue with coronary artery disease. *Int J*
946 *Cardiol* **324**, 152–164 (2021).

947 79. Ghigo, A., Laffargue, M., Li, M. & Hirsch, E. PI3K and Calcium Signaling in Cardiovascular Disease.
948 *Circ Res* **121**, 282–292 (2017).

949 80. Ghigo, A., Morello, F., Perino, A. & Hirsch, E. Therapeutic Applications of PI3K Inhibitors in
950 Cardiovascular Diseases. *Future Med Chem* **5**, 479–492 (2013).

951 81. Qin, W., Cao, L. & Massey, I. Y. Role of PI3K/Akt signaling pathway in cardiac fibrosis. *Molecular*
952 *and Cellular Biochemistry 2021 476:11* **476**, 4045–4059 (2021).

953 82. Chong, Z. Z., Shang, Y. C. & Maiese, K. Cardiovascular Disease and mTOR Signaling. *Trends*
954 *Cardiovasc Med* **21**, 151–155 (2011).

955 83. Yang, Z. & Ming, X. F. mTOR signalling: the molecular interface connecting metabolic stress, aging
956 and cardiovascular diseases. *Obesity Reviews* **13**, 58–68 (2012).

957 84. Sciarretta, S., Forte, M., Frati, G. & Sadoshima, J. New Insights Into the Role of mTOR Signaling in
958 the Cardiovascular System. *Circ Res* **122**, 489–505 (2018).

959 85. Samidurai, A., Kukreja, R. C. & Das, A. Emerging role of mTOR signaling-related miRNAs in
960 cardiovascular diseases. *Oxid Med Cell Longev* **2018**, (2018).

961 86. Das, A. & Reis, F. mTOR Signaling: New Insights into Cancer, Cardiovascular Diseases, Diabetes
962 and Aging. *International Journal of Molecular Sciences 2023, Vol. 24, Page 13628* **24**, 13628
963 (2023).

964 87. Ghafouri-Fard, S. *et al.* Interplay between PI3K/AKT pathway and heart disorders. *Mol Biol Rep*
965 **49**, 9767–9781 (2022).

966 88. Shen, A. R. *et al.* Integrin, Exosome and Kidney Disease. *Front Physiol* **11**, 627800 (2021).

967 89. van den Hoogen, P. *et al.* Increased circulating IgG levels, myocardial immune cells and IgG
968 deposits support a role for an immune response in pre- and end-stage heart failure. *J Cell Mol*
969 *Med* **23**, 7505–7516 (2019).

970 90. Tsimikas, S. *et al.* Relationship of IgG and IgM autoantibodies to oxidized low density lipoprotein
971 with coronary artery disease and cardiovascular events. *J Lipid Res* **48**, 425–433 (2007).

972 91. Ronan, G., Bahcecioglu, G., Yang, J. & Zorlutuna, P. Cardiac tissue-resident vesicles differentially
973 modulate anti-fibrotic phenotype by age and sex through synergistic miRNA effects. *Biomaterials*
974 **311**, (2024).

975 92. Chen, Y. & Wang, X. miRDB: an online database for prediction of functional microRNA targets.
976 *Nucleic Acids Res* **48**, D127 (2019).

977 93. Huang, H. Y. *et al.* miRTarBase update 2022: an informative resource for experimentally validated
978 miRNA–target interactions. *Nucleic Acids Res* **50**, D222 (2021).

979 94. Agarwal, V., Bell, G. W., Nam, J. W. & Bartel, D. P. Predicting effective microRNA target sites in
980 mammalian mRNAs. *Elife* **4**, e05005 (2015).

981 95. Ashburner, M. *et al.* Gene ontology: tool for the unification of biology. The Gene Ontology
982 Consortium. *Nat Genet* **25**, 25–29 (2000).

983 96. Consortium, G. O. The Gene Ontology resource: enriching a GOld mine. *Nucleic Acids Res* **49**,
984 D325–D334 (2021).

985 97. Mi, H., Muruganujan, A., Ebert, D., Huang, X. & Thomas, P. D. PANTHER version 14: more
986 genomes, a new PANTHER GO-slim and improvements in enrichment analysis tools. *Nucleic Acids*
987 *Res* **47**, D419–D426 (2019).

988 98. Liebermeister, W. *et al.* Visual account of protein investment in cellular functions. *Proc Natl Acad*
989 *Sci U S A* **111**, 8488–8493 (2014).

990 99. Tibshirani, R. Regression Shrinkage and Selection Via the Lasso. *J R Stat Soc Series B Stat*
991 *Methodol* **58**, 267–288 (1996).

992 100. Fan, J. & Li, R. Variable Selection via Nonconcave Penalized Likelihood and its Oracle Properties. *J*
993 *Am Stat Assoc* **96**, 1348–1360 (2001).

994 101. van Hoogevest, P. & Wendel, A. The use of natural and synthetic phospholipids as
995 pharmaceutical excipients. *European Journal of Lipid Science and Technology* **116**, 1088 (2014).

996 102. Le, N. T. T. *et al.* Soy Lecithin-Derived Liposomal Delivery Systems: Surface Modification and
997 Current Applications. *Int J Mol Sci* **20**, 4706 (2019).

998 103. Wang, G. & Wang, T. Oxidative stability of egg and soy lecithin as affected by transition metal
999 ions and pH in emulsion. *J Agric Food Chem* **56**, 11424–11431 (2008).

1000 104. Yanasarn, N., Sloat, B. R. & Cui, Z. Nanoparticles Engineered from Lecithin-in-Water Emulsions As
1001 A Potential Delivery System for Docetaxel. *Int J Pharm* **379**, 174 (2009).

1002 105. Cornejo, M. A. & Linz, T. H. Selective miRNA quantitation with high-temperature thermal gel
1003 electrophoresis. *Anal Chim Acta* **1275**, 341605 (2023).

1004 106. Guo, M., Wei, Y., Lee, H., Maia, J. & Morrison, E. One-step extrusion of concentrated lidocaine
1005 lipid nanocarrier (LNC) dispersions. *Int J Pharm* **589**, 119817 (2020).

1006 107. Basara, G., Gulberk Ozcebe, S., Ellis, B. W. & Zorlutuna, P. Tunable human myocardium derived
1007 decellularized extracellular matrix for 3d bioprinting and cardiac tissue engineering. *Gels* **7**,
1008 (2021).

1009

1010 **ACKNOWLEDGEMENTS**

1011 We thank Dr. Kieth March for providing the plasma samples utilized in this study.

1012 The lyophilization of decellularized ECM was conducted at the Center for Environmental Science
1013 and Technology (CEST) at the University of Notre Dame.

1014 We thank the Biophysics Instrumentation (BIC) Core Facility for the use of Optima MAX-XP
1015 Tabletop Ultracentrifuge.

1016 The authors acknowledge the use of the Electron Microscopy Core of the Notre Dame Integrated
1017 Imaging Facility, a designated core of the NIH-funded Indiana Clinical and Translational Sciences
1018 Institute.

1019 The Nanoparticle Tracking Analysis was conducted using the NanoSight NS300 at the Harper
1020 Cancer Research Institute (HCRI) Tissue Core Facility.

1021 **Funding:** Research reported in this publication was supported by NSF-CAREER Award #
1022 1651385, NSF CBET Award # 1805157 and NIH Award # 1 R01 HL141909-01A1

1023 **Competing Interests Statement:** The authors have no competing interest to disclose.

1024 **Data Availability Statement:** All data required for production of the manuscript is included in
1025 this submission. Additional raw data can be provided upon request.

1026 **Ethics Statement:** Human heart tissue was collected from donors whose hearts were deemed
1027 unsuitable for transplantation through the Indiana Donor Network (IDN) or National Disease
1028 Research Institute (NDRI). IRB approval was waived, as no identifying information was provided
1029 by the Indiana Donor Network or NDRI. De-identified human whole blood was collected from
1030 live donors at the University of Florida College of Medicine through an IRB approved standard
1031 collection protocol (IRB#201901232). All tissue collection was performed in accordance with the
1032 declaration of Helsinki.